

Title	Novel approaches for genuine single phase room temperature magnetoelectric multiferroics
Authors	Keeney, Lynette;Schmidt, Michael;Amann, Andreas;Maity, Tuhin;Deepak, Nitin;Faraz, Ahmad;Petkov, Nikolay;Roy, Saibal;Pemble, Martyn E.;Whatmore, Roger W.
Publication date	2016-05
Original Citation	Keeney, L. , Schmidt, M. , Amann, A. , Maity, T. , Deepak, N. , Faraz, A. , Petkov, N. , Roy, S. , Pemble, M. E. and Whatmore, R. W. (2016) 'Novel Approaches for Genuine Single-Phase Room Temperature Magnetoelectric Multiferroics', in Algueró, M., Gregg, J. M. and Mitoseriu, L. (eds). Nanoscale Ferroelectrics and Multiferroics, London: John Wiley & Sons, Ltd, pp. 789-829. doi: 10.1002/9781118935743.ch25
Type of publication	Book chapter
Link to publisher's version	https://onlinelibrary.wiley.com/doi/10.1002/9781118935743.ch25 - 10.1002/9781118935743.ch25
Rights	© 2016 John Wiley & Sons, Ltd. All rights reserved. This is the accepted version of the following chapter which has been published in final form at https://doi.org/10.1002/9781118935743.ch25 .
Download date	2025-07-02 13:56:35
Item downloaded from	https://hdl.handle.net/10468/7729



UCC

University College Cork, Ireland
Coláiste na hOllscoile Corcaigh

Chapter 21. Novel approaches for genuine single phase room temperature magnetoelectric multiferroics

Lynette Keeney¹, Michael Schmidt¹, Andreas Amann^{1,2}, Tuhin Maity¹, Nitin Deepak¹, Ahmad Faraz¹, Nikolay Petkov¹, Saibal Roy¹, Martyn E. Pemble^{1,3} and Roger W. Whatmore^{1,3,4}

¹*Tyndall National Institute, University College Cork, Cork, Ireland*

²*School of Mathematical Sciences, University College Cork, Cork, Ireland*

³*Department of Chemistry, University College Cork, Cork, Ireland*

⁴*Department of Materials, Royal School of Mines, Imperial College London, South Kensington Campus, London SW7 2AZ*

With the seemingly inexorable increase in the use of devices designed to access the internet for an ever increasing series of applications, there is a constant need for data storage technologies with higher densities, non-volatility and lower power consumption.³ Single-phase, room temperature magnetoelectric multiferroic materials are of considerable interest for such applications.⁴ The unique advantage of these advanced materials is that not only could they find application in high storage density, low-power memory devices that can be electrically written and magnetically read, but also by constructing devices that exploit the presence of both ferroelectric and ferromagnetic states, memory technologies with 4-state logic could be achieved⁵ - representing a clear improvement over current 2-state logic memory. However, materials that are both multiferroic and magnetoelectric at room temperature are very unusual.⁶ In this chapter, we review approaches currently under investigation for the fabrication of single phase magnetoelectric multiferroics, from bulk ceramics to those in thin film form. We present

an approach of inserting magnetic ions into Aurivillius phase, layer-structured ferroelectric materials, whereby thin films of average composition $\text{Bi}_6\text{Ti}_{2.8}\text{Fe}_{1.52}\text{Mn}_{0.68}\text{O}_{18}$ demonstrate room temperature ferroelectricity, ferromagnetism and magnetoelectric coupling.² We discuss the importance of careful microstructural analysis of the materials and the application of a statistical model to determine a confidence level that the observed effects are from genuine single-phase magnetoelectric multiferroics and do not originate from unobserved second phase ferromagnetic inclusions.

EXPANDED INDEX:

21.1. Introduction to Single Phase Multiferroic Materials

Examples of current single phase multiferroic materials are presented. While low temperature multiferroics exist, the rarity of room temperature multiferroics is discussed. Current theoretical and experimental approaches into the design of potential room temperature single phase magnetoelectric multiferroics are reviewed.

21.2. Aurivillius Phase Materials - Candidate Single Phase Multiferroics?

The Aurivillius phase family of materials is presented as an approach for potential achievement of single phase multiferroicity. Previous reports of ferroelectricity and ferromagnetism / antiferromagnetism in the Aurivillius phases are reviewed.

21.3. Magnetoelectric Coupling in Multiferroic $\text{Bi}_6\text{Ti}_x\text{Fe}_y\text{Mn}_z\text{O}_{18}$ Systems at Room Temperature

21.3.1 Fabrication and Structural Analysis of $\text{Bi}_{m+1}\text{Ti}_3(\text{Mn/Fe})_{m-3}\text{O}_{3m+1}$ Thin Films An approach for increasing the magnetic cation content in the Aurivillius phases by synthesising $\text{Bi}_{m+1}\text{Ti}_3\text{Fe}_m$.

O_{3m+1} thin films where $m \geq 5$ and novel materials substituted with Mn cations is presented. The effect of Ti/Fe/Mn compositional ratios on the Aurivillius phase structures is discussed.

21.3.2 Ferroelectric Investigations of $\text{Bi}_6\text{Ti}_x\text{Fe}_y\text{Mn}_z\text{O}_{18}$ Thin Films

Ferroelectric switching investigations of the $\text{Bi}_6\text{Ti}_x\text{Fe}_y\text{Mn}_z\text{O}_{18}$ films are presented.

21.3.3 Assessment of Ferromagnetism in $\text{Bi}_6\text{Ti}_x\text{Fe}_y\text{Mn}_z\text{O}_{18}$ Thin Films

Magnetic investigations of the $\text{Bi}_6\text{Ti}_x\text{Fe}_y\text{Mn}_z\text{O}_{18}$ films are presented and a mechanism for the ferromagnetism is proposed.

21.3.4 Room Temperature Magnetoelectric Coupling in $\text{Bi}_6\text{Ti}_{2.8}\text{Fe}_{1.52}\text{Mn}_{0.68}\text{O}_{18}$ Thin Films

Direct evidence for magnetoelectric coupling in multiferroic $\text{Bi}_6\text{Ti}_{2.8}\text{Fe}_{1.52}\text{Mn}_{0.68}\text{O}_{18}$ thin films at room temperature is demonstrated.

21.4. Confidence Level Assessment of Genuine Single Phase Multiferroicity

An assessment of the prospect of observed multiferroic properties being intrinsic to the main phase in a given sample is discussed. A dedicated statistical model applied to the design of the analytical measurements is shown and its application to the analysis of thin films is demonstrated to put a high, defined confidence level ($> 99.5\%$) to the statement of a material being a ‘new single phase multiferroic material’.⁷

21.5. Potential devices / applications based on single phase magnetoelectric multiferroics

The potential device-type structures incorporating single phase magnetoelectric multiferroics are considered as prospective architectures for memory scaling beyond current technologies.

21.6. Summary and conclusions

21.7 References

21.1 Introduction to Single Phase Multiferroic Materials

To illustrate the unique potential of single phase multiferroic materials, it is important to clarify the distinction between *magnetoelectric* materials and *multiferroic* materials:

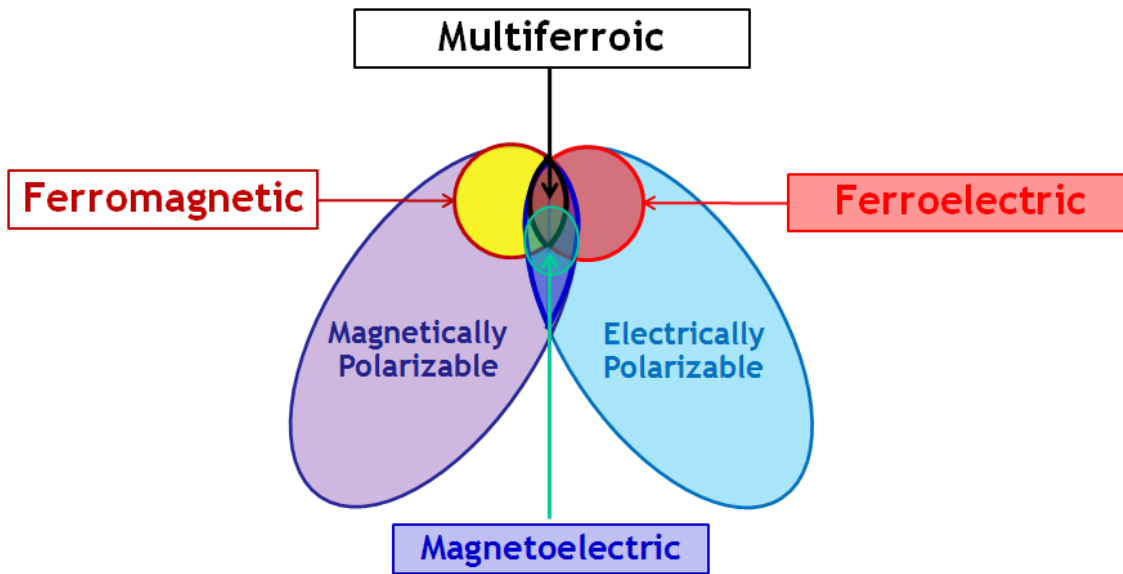


Fig. 1.1. The relationship between multiferroic and magnetoelectric materials. (Redrawn from^{1,2}).

Electrically polarisable materials possess an electrical dipole moment which can be affected by an external electric field and magnetically polarisable materials possess magnetic dipole moments which are affected by an external magnetic field. As illustrated in the Venn diagram in **Figure 1.1**, **magnetoelectric** materials are those where there is coupling between electric and magnetic order parameters such that magnetisation can be induced by an electric field and vice versa. This may arise through direct coupling between magnetic and electric polarizations in a single material (e.g. Cr_2O_3 , magnetoelectric below 260 K)⁸, or indirectly via

strain-mediated coupling in a multi-phase material (e.g. CoFe-BaTiO₃ heterostructures)⁹. Examples of single-phase magnetoelectrics include: Cr₂O₃ (<260 K)⁸, CuO (<230 K)¹⁰, TbMnO₃ (<27 K)¹¹, Ni₃B₇O₁₃I (<64 K)¹², DyMn₂O₅ (<43 K)¹³. Strain-mediated indirect magnetoelectric coupling in composite materials can occur, for example, through a magnetostrictive strain (induced in one phase by a change in applied magnetic field) coupling to a piezoelectrically-induced polarization change in a second phase mechanically-coupled to the first. The SI unit of the magnetoelectric coupling coefficient, α , is [sm⁻¹] which can be converted to the technical unit [Vcm⁻¹Oe⁻¹] if the permittivity (ϵ) of the given material is known: [sm⁻¹] = 1.1 x 10⁻¹¹ ϵ [Vcm⁻¹Oe⁻¹]. A magnetoelectric coupling coefficient of 5.90 Vcm⁻¹Oe⁻¹ has been reported for laminate complexes of lead zirconate titanate (PZT) and Terfenol-D (TbDyFe₂) by straining the magnetostrictive phase under a DC magnetic bias of 4.2 T,¹⁴ which induces stress on the piezoelectric phase, generating an electric field in the piezoelectric phase. Magnetic force microscopy imaging of (BiFeO₃)_{0.65}-(CoFe₂O₄)_{0.35} nanostructured composite heterostructures¹⁵, demonstrated two electrically-switchable perpendicular magnetic states at ambient conditions for ferromagnetic CoFe₂O₄ nanopillars embedded in BiFeO₃. Additionally, the magnetoelectric coupling effect becomes controllable in a weak perpendicular magnetic field. Thin film heterostructures⁹ of CoFe-BaTiO₃ grown by electron-beam evaporation exhibit giant magnetoelectric coupling coefficients (3 x 10⁻⁶ sm⁻¹) at room temperature. Lahtinen *et al.* demonstrated that it is possible to precisely write and erase regular ferromagnetic domain patterns and to control the motion of magnetic domain walls in small electric fields over large areas in these composites by strain-mediated correlations between ferromagnetic domain walls and ferroelastic domain boundaries.

An important subset of the electrically polarisable materials is the **ferroelectrics**, whose dipole moments can not only be switched by an applied electric field, but also their polarisation states remain even when the electric field is removed. This is the basis for non-volatile ferroelectric random access memory, where polarisation states are encoded into computer bits at fast writing performances which retain their memory states when the computer is powered-off. Similarly, the **ferromagnets** are a subset of magnetically polarisable materials such that their magnetic dipole moments align in a magnetic field to give a resultant magnetic moment which is retained when the magnetic field is removed. Ferromagnetic materials are used as recording media in hard disc drives and have increased storage capacity over ferroelectric materials. Spin Transfer Torque Magnetic Random Access Memory (STT-MRAM) has been road-mapped as an emerging memory technology.¹⁶ However, a current drawback of ferromagnetic memory is the considerable power that is usually required for magnetic writing.

As **Figure 1.1** illustrates, materials which demonstrate both ferroelectric and ferromagnetic properties *within the same phase* are known as ***multiferroic*** materials. The term “multiferroic” refers to any material in which more than one ferroic effect (ferroelectricity, ferromagnetism, ferroelasticity) exists in the same phase. *Magnetoelectricity*, on the other hand, is an independent phenomenon that can arise in any material whatever the nature of magnetic and electrical order parameters, regardless of whether it is multiferroic or not¹⁷. For example, the first magnetoelectric discovered, Cr₂O₃ is neither ferroelectric nor ferromagnetic.¹⁸ Since the switched states in this material are transient and do not persist, magnetoelectric materials of this type are inadequate for memory storage applications.

In this regard the synthesis of novel room temperature ***single-phase magnetoelectric multiferroic*** materials is particularly appealing, because the magnetoelectric and multiferroic

coupling interactions could create a range of potential applications. These materials could potentially lead to a new generation of **rapid, energy efficient** memory devices with **increased data storage densities** based on the combined advantages of ferroelectric and ferromagnetic memory. The fabrication of magnetoelectric memory devices that can be *electrically written and magnetically read* as well as magnetic field sensors where the ferromagnetic resonance could be tuned electrically instead of magnetically are promising avenues for exploitation in technologies **requiring reduced energy consumption** applications.^{19, 20} The *unique commercial potential* of the B6TFMO thin films lies in the opportunity for the creation of a **4-state memory technology** using the combination of simultaneous ferroelectric and ferromagnetic polarisation states (positive and negative in both electrical and magnetic polarizations). The fabrication of memory devices with storage of **multiple bits per memory element** would significantly *advance data storage capabilities* to meet consumer demand for increasingly higher data density. Therefore, the design and identification of new mechanisms that can lead to multiferroic magnetoelectric coupling behaviour is in demand.

However, until very recently, there were no single-phase ferroelectric/ferromagnetic multiferroics at room temperature. One reason for the scarcity of single-phase multiferroics is the competing electronic requirements for ferroelectricity and ferromagnetism²¹. Hybridization between the cation and anion within the unit cell is the conventional mechanism for stabilizing non-centrosymmetric ferroelectric distortion; therefore the cation driving ferroelectricity must formally be in the d^0 state. Conversely, d -orbital occupancy is a requirement for the existence of magnetic ordering. Hill²¹ has suggested that the conditions for obtaining ferroelectricity and ferromagnetism in a single phase can potentially be met by incorporating d^0 and d^n cations into the same structure or where stereochemical activity of the A-site lone pair gives rise to

ferroelectricity and magnetism arises from the *B*-site cation. Multiferroic materials generated by this type of pathway, where ferroelectricity and ferromagnetism have different sources, are classified as **Type I multiferroics**. Generally, ferroelectric ordering temperatures tend to be higher than the magnetic ordering temperature and coupling between electric and magnetic order parameters tends to be weak in this class of multiferroics. Note that given that there are so few ferromagnetic ferroelectrics, the current trend is to extend the definition of multiferroic materials to include materials possessing the corresponding antiferroic properties such as antiferroelectricity/antiferromagnetism.²² Examples of multiferroic materials which arise from *lone-pair effects* are the extensively studied^{17, 22, 23, 24, 25, 26, 27, 28, 29, 30} room temperature ferroelectric (T_c 110K)/antiferromagnetic (T_N 643K) BiFeO₃ (which also displays a weak canted ferromagnetic moment) and BiMnO₃^{31, 32, 33}, which is a ferromagnetic oxide ($T_c = \sim 105$ K) reported to be ferroelectric ($T_c = \sim 450$ K). Despite the electronic limitations, several multiferroics have been discovered wherein ferroelectricity is induced by clever routes, including a second group of materials in this class called the *geometrically driven* multiferroics, where ferroelectricity results from long-range dipole-dipole interactions and oxygen rotations.²³ For example, ferroelectricity ($T_c \sim 914$ K) in YMnO₃ is driven by from polyhedral tilting of the MnO₅ block and is compatible with the coexistence of antiferromagnetism ($T_N \sim 80$ K).^{34, 35, 36} A third route to multiferroism in this class is provided by non-centrosymmetric *charge ordering* in magnetic materials.²⁴ This can be seen in compounds containing transition metals e.g. LuFe₂O₄ (ferroelectric $T_c \sim 330$ K and ferromagnetic $T_c \sim 250$ K)^{37, 38} with formally different valence or bond lengths where formation of inequivalent sites can lead to ferroelectricity. In **Type II multiferroics**, ferroelectricity is induced by *magnetic ordering* and the formation of a symmetry-lowering magnetic ground state that lacks inversion symmetry. Since magnetism causes

ferroelectricity, there tends to be a strong coupling between order parameters, however ferroelectric polarization tends to be small.²⁴ In TbMnO_3 , frustrated magnetism and spiral magnetic ordering ($T_N \sim 41\text{K}$) is accompanied by a magnetoelastically induced lattice distortion, which in turn induces ferroelectricity ($T_C \sim 27\text{K}$).¹¹ Despite research of other materials in this class e.g. TbMn_2O_4 ($T_N \sim 43\text{K}$ and $T_C \sim 38\text{K}$)³⁹ and DyMnO_3 ($T_N \sim 38\text{K}$ and $T_C \sim 18\text{K}$)⁴⁰, the discovery of a rare earth manganite that demonstrates both room temperature ferroelectricity and ferromagnetism still remains.³²

Advances in thin film growth techniques have allowed the production of high quality ultra-thin films where ‘*strain tuning*’ can induce ferroelectric polarisation^{41, 42}, can lead to a significant increase of the spontaneous polarization⁴³ and can compensate the adverse influence of thickness reduction and preserve ferroelectricity in ultra-thin perovskite films⁴⁴. Sando et al.,²⁷ investigated the effect of -2.6% (compressive) to +1.3% (tensile) strain on pulsed laser deposition (PLD) grown thin films of BiFeO_3 (50-70nm) on substrates ranging from $(\text{LaAlO}_3)_{0.3}-(\text{Sr}_2\text{AlTaO}_6)_{0.7}$ to PrScO_3 . It was found that high epitaxial strain destroys the bulk-like cycloidal modulation; however the antiferromagnetic state is stable at high compressive strain. There is a progressive reorientation of magnetic spins from in-plane to out-of-plane as the strain is changed from compressive to tensile, and the authors demonstrate how epitaxial strain in BiFeO_3 can tune the exchange bias and giant-magnetoresistive response of CoFeB/Cu/Co spin valves.²⁷

First principle calculations have predicted that *epitaxial strain* can provide a route to multiferroicity in epitaxial thin films and may lead to an increase ferromagnetic Curie temperature.^{45, 46, 47, 48} The paraelectric ferromagnet EuO (T_C 69K) is predicted⁴⁶ to become ferroelectric under epitaxial strain. A compressive strain of -5.5% is anticipated to yield a polarization of $60 \mu\text{Ccm}^{-2}$ in the out-of-plane direction and in-plane polarization is predicted

under tensile strain while the ferromagnetic state remains unchanged. If a system has a spin-phonon coupling in which the lowest-frequency polar phonon is softer for ferromagnetic ordering than for antiferromagnetic ordering, then epitaxial strain enhancement of a polar instability is expected to decrease the energy of the ferromagnetic-ferroelectric state relative to that of the antiferromagnetic-paraelectric state.⁴⁸ Via this mechanism, density functional theory calculates that both tensile ($+4.5 \pm 1\%$) and compressive ($-4.9 \pm 2\%$) strain can drive antiferromagnetic-paraelectric SrMnO_3 system through a series of phase transitions to a ferromagnetic ($T_c > 92 \text{ K}$) – ferroelectric ($P_s > 54 \mu\text{Ccm}^{-2}$) multiferroic state.⁴⁸ Fennie et al.⁴⁷ proposed a spin-phonon coupling mechanism for epitaxial strain transformation of EuTiO_3 , an antiferromagnetic-paraelectric insulator in un-strained form, into a single phase ferroelectric ($P \sim 10 \mu\text{Ccm}^{-2}$) – ferromagnet ($7 \mu_B$) in epitaxial thin films compressively strained above -1.25% . Strong coupling between magnetic and ferroelectric ordering is realised with spin-phonon coupling through which ferromagnetic spin-alignment softens a low-frequency polar mode which is strongly coupled to biaxial epitaxial strain.^{47, 49} Whereas ferromagnetic-ferroelectric multiferroicity remains to be demonstrated experimentally in EuO and SrMnO_3 , Lee et al.⁵⁰ were successful in verifying that spin-lattice coupling converts EuTiO_3 into a ferromagnetic-ferroelectric multiferroic. Due to the lack of a suitable substrate to allow for the appropriate biaxial compressive strain (-1.25 to -2%), they calculated that the critical tensile strain to reach the ferroelectric-ferromagnetic ground state of EuTiO_3 is $+0.75\%$. 22 nm (001)-oriented EuTiO_3 films grown by reactive molecular beam epitaxy on (110) DyScO_3 substrates (strain = $+1.1\%$) demonstrated ferroelectricity below $T_c \sim 250\text{K}$ and ferromagnetism below $T_c 4.24 \pm 0.02\text{K}$ and capacitance measurements demonstrate that the two order parameters are coupled, however,

unfortunately this magnetoelectric multiferroic phase is only observed at very low temperatures.⁵⁰

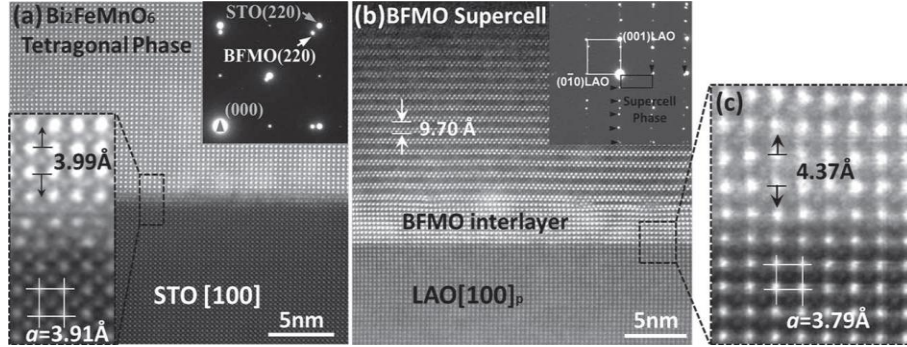


Fig. 1.2. Scanning transmission electron microscopy (STEM) images of (a) Bi₂FeMnO₆ structure obtained on SrTiO₃(001) and (b) the new Bi₃Fe₂Mn₂O_x (BFMO322) supercell structure obtained on LaAlO₃ substrates. (c) Displays the increased magnification image of the region outlined in (b) demonstrating the coherent interface between the LaAlO₃ substrate and the BFMO interlayer. From Chen *et al.*⁵¹

Chen *et al.*⁵¹ have demonstrated that substrate-induced epitaxial strain is a valuable approach to the formation of new structures with additional functionality which cannot be grown as equilibrium single crystals. Under identical pulsed laser deposition conditions, thin films of the conventional pseudo-perovskite Bi₂FeMnO₆ structure were obtained on SrTiO₃(001) substrates (**Fig. 1.2(a)**), while growth on LaAlO₃(001) substrates yielded the new Bi₃Fe₂Mn₂O_x (BFMO322) supercell structure (**Fig. 1.2(b)** and (c)) which demonstrates ferroelectric (P_r (remanent polarization) = $6 \mu\text{C}/\text{cm}^2$, d_{33} (piezoelectric coefficient) $\sim 30 \text{ pmV}^{-1}$) and ferromagnetic (M_s (saturated magnetization) $\sim 110 \text{ emu}/\text{cm}^3$) properties at room temperature. This BFMO322

supercell, with a cation ratio of Bi:Fe:Mn = 3:2:2, is related to the Aurivillius⁵² phases and its formation is strongly substrate dependent. A lattice misfit of -2.0% enables growth on LaAlO₃ whereas no growth occurs on SrTiO₃ (lattice misfit is -0.6%).⁵¹ Abberation corrected scanning transmission electron microscopy (Cs-corrected STEM) and optimized geometric phase analysis (GPA) establishes that the formation of biaxial lattice strain distributions and highly strained BFMO transition layers between the LaAlO₃ substrate and the BFMO322 supercell are crucial for triggering the growth of the BFMO322 supercell structure.⁵³ As the thickness of the BFMO interlayers increases, the elastic biaxial strain increases up to thicknesses of ~3-4 nm, whereupon interfacial defects consisting of misfit dislocation partials are generated to relax the mismatch strain. This is followed by the growth of the BFMO322 supercell which is partially relaxed to ~3.7-4.4% (compared with Bi₂FeMnO₆ on SrTiO₃ with a relative strain of -0.33%). The film crystal structure and stoichiometry evolve gradually from the highly distorted pseudo-perovskite structure to the BFMO322 supercell through the interfacial phases, demonstrating that *heteroepitaxial strain* is progressing as a new route for the generation of multiferroic phases.⁵³

Chemical control of functionality on a site-by site basis is possible with *multi-component oxide systems*. The hexaferrite Sr₃Co₂Fe₂₄O₄₁ demonstrates low-field magnetoelectric effects at room temperature, however shows no polarization at zero magnetic field and therefore is not a bilinear magnetoelectric.⁵⁴ SrCo₂Ti₂Fe₈O₁₉ does exhibit spontaneous polarization at zero magnetic field ($\sim 25 \mu\text{Ccm}^{-2}$)⁵⁵ and decreases in magnetization of up to 6.3% on application of a magnetic field of 46mT and E_{dc} of 22 kv/cm. Magnetic force microscopy investigations of this ceramic under various electric fields (E_{dc} ~ -20 to +20 kv/cm) demonstrated decreases in magnetic contrast and electric-field control of magnetism at room temperature in the absence of a

magnetic field bias (converse magnetoelectric effect), however no change in domain structure could be detected.

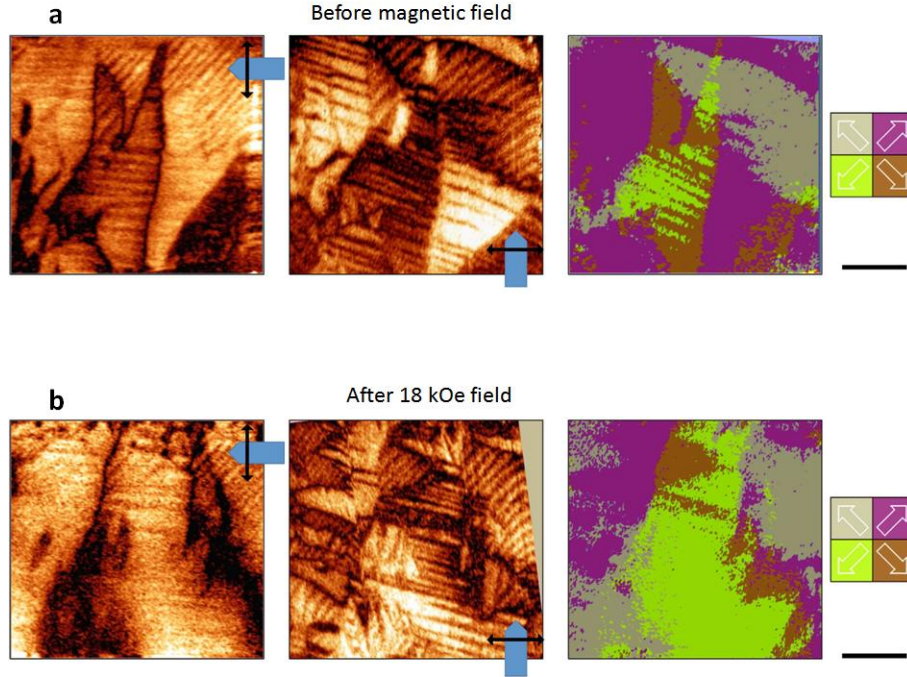


Fig. 1.3. Ferroelectric domain configurations of $[\text{Pb}(\text{Zr}_{0.53}\text{Ti}_{0.47})\text{O}_3]_{0.6}-[\text{Pb}(\text{Fe}_{0.5}\text{Ta}_{0.5})\text{O}_3]_{0.4}$ changing dramatically with an applied magnetic field.⁵⁶ Lateral piezoresponse force microscopy images before (a) and after (b) the application of 1.8 T magnetic field.

Recently, a newly-discovered single-phase multiferroic, $[\text{Pb}(\text{Zr}_{0.53}\text{Ti}_{0.47})\text{O}_3]_{0.6}-[\text{Pb}(\text{Fe}_{0.5}\text{Ta}_{0.5})\text{O}_3]_{0.4}$ has been shown to exhibit dramatic changes to ferroelectric domain configurations on application of applied magnetic fields (-0.3 to +1.8 T) (**Fig. 1.3**) and significant (~60% change in polarization) bilinear magnetoelectric coupling in lamellae of the ceramic at room temperature ($\sim 1 \times 10^{-7} \text{ sm}^{-1}$).^{27, 57, 58} In addition, magnetic and dielectric anomalies appear at similar temperatures to the elastic data, giving further indications that the

multiple ferroic order parameters are strongly coupled.⁵⁸ Evans *et al.*⁵⁶ put forward a strain-mediated coupling mechanism for these observations of ferroelectric domain switching in $[\text{Pb}(\text{Zr}_{0.53}\text{Ti}_{0.47})\text{O}_3]_{0.6}-[\text{Pb}(\text{Fe}_{0.5}\text{Ta}_{0.5})\text{O}_3]_{0.4}$ on application of a magnetic field.

For a period in the 2000s, there had been a number of contradictory studies^{30, 59, 60} on the multiferroic properties of BiFeO_3 thin films. Wang *et al.*³⁰ reported an enhancement of room temperature ferromagnetism ($\sim 150 \text{ emu/cm}^3$ or $\sim 1 \mu_{\text{B}}/\text{Fe}$) in 70 nm heteroepitaxially strained films compared with the weak ferromagnetism expressed in bulk BiFeO_3 . However Béa *et al.*⁶¹ demonstrated that the large ferromagnetic moment was not as a result of epitaxial strain in the films, rather, virtually all of the ferromagnetic signal observed in BiFeO_3 thin films could be attributed to the presence of ferrimagnetic $\gamma\text{-Fe}_2\text{O}_3$ (magnetic moment $\sim 420 \text{ emu/cm}^3$ or $1.25 \mu_{\text{B}}/\text{Fe}$) precipitates. This parasitic $\gamma\text{-Fe}_2\text{O}_3$ phase was detectable and quantifiable by x-ray absorption spectroscopy (XAS) and x-ray magnetic circular dichroism (XMCD); however it was not easily detectable by the less sensitive X-ray diffraction technique. The intrinsic magnetization of BiFeO_3 , without detectable parasitic phases, is confirmed to be low ($\leq 0.02 \mu_{\text{B}}/\text{Fe}$).⁶¹ This work demonstrates the importance of detailed phase analysis when designating materials as room temperature ferroelectric/ferromagnetic multiferroics.

By inserting magnetic ions into lead-free layered-structured ferroelectric materials in the Aurivillius phase, we outline (Section 21.3 to Section 21.6) how Keeney *et al.*² were successful in synthesising thin films of average composition, $\text{Bi}_6\text{Ti}_{2.8}\text{Fe}_{1.52}\text{Mn}_{0.68}\text{O}_{18}$ (B6TFMO), which demonstrate ferroelectric and ferromagnetic properties at room temperature. Given that trace levels of magnetic impurity inclusions can significantly affect the observed ferromagnetic response from the main phase^{30, 61, 62, 63}, Section 21.4 reviews how careful phase analysis and statistical treatment of the data confirmed that B6TFMO phase is a single phase multiferroic to a

confidence level of 99.5%. Section 21.3.4 summarises how direct evidence of magnetoelectric coupling in the B6TFMO thin films was obtained. This review demonstrates that with materials development and design, the development of room temperature multiferroic materials can be achieved.

21.2 Aurivillius Phase Materials - Candidate Single Phase Multiferroics?

The layered-structured Aurivillius phase materials (**Fig. 2.1**),⁵² described by the general formula $\text{Bi}_2\text{O}_2(\text{A}_{m-1}\text{B}_m\text{O}_{3m+1})$, are a particularly attractive class of oxides for the design of prospective new single phase multiferroic systems as they offer the potential to include substantial amounts of magnetic cations within a strongly ferroelectric system. The materials are members of an homologous family of Bi-layered oxides, where the structure is a naturally layered nano-composite. The 2-dimensional nano-structures have large c -axis lattice parameters (the stacking axis), in the nanometer range, and consist of fluorite-structured $(\text{Bi}_2\text{O}_2)^{2+}$ layers of thickness f (typically $\sim 0.4\text{nm}$) lying in the (001) plane. These phases are very flexible, as between the bismuth oxide layers, a wide range of B -site cations can be sandwiched in the form of $m\text{ABO}_3$ perovskite-type layers. The number of ABO_3 perovskite units (m) per half unit cell can be altered within the range 1 to 9, depending on composition, and a variety of over 50 Aurivillius phase compounds have been reported.^{64, 65, 66, 67} In **Fig. 2.1.**, one unit of BiFeO_3 has been inserted into $\text{Bi}_4\text{Ti}_3\text{O}_{12}$ to form the four-layered material, $\text{Bi}_5\text{Ti}_3\text{FeO}_{15}$. The average thickness of the perovskite-type block, h , is influenced by the number of octahedral perovskite units (m) in the block: $h = pm$ where p is the average thickness of the perovskite-like units (also typically $\sim 0.4\text{nm}$).⁶⁸ (Note that this is only an approximation, as octahedral tilting, and choice of A & B cations will change the average height of each perovskite unit.^{69, 70, 71}) The value of m can be an integer or fractional.⁷² Fractional values of m usually occur with “mixtures” between a pure Aurivillius phase compound and a perovskite end member. These are formed by recurrent intergrowth of the perovskite blocks of two Aurivillius end-members, eg. $\text{BaBi}_8\text{Ti}_7\text{O}_{27}$ ($m = 3.5$) is formed from $(\text{Bi}_4\text{Ti}_3\text{O}_{12})_{0.75}-(\text{BaTiO}_3)_{0.25}$.^{73, 74} The values of f and h are related to the c cell parameter by $f + h = c/2$. **Table 2.1.** demonstrates that this formula fits quite well for a variety of Aurivillius phase

compositions, and it provides a reasonable model from which the values of m can be obtained for any Aurivillius compound.

Table 2.1. Comparison of c -lattice parameter predicted by $f + h = c/2$ with that obtained from diffraction data for Aurivillius phase compositions of $m = 2-4$. Where $h = pm$ and values of 4.11Å and 4.08Å for p and f respectively, were used for the prediction.

Aurivillius phase	m	c (Å) predicted	c (Å) obtained
SrBi ₂ Ta ₂ O ₉	2	24.60	25.02641(50) ⁷⁵
(Bi ₃ TiNbO ₉) _{0.5} –(Bi ₄ Ti ₃ O ₁₂) _{0.5}	2.5	28.71	29.05 ⁷⁶
Bi ₄ Ti ₃ O ₁₂	3	32.82	32.8111(4) ⁷⁷
BaBi ₈ Ti ₇ O ₂₇	3.5	36.93	37.198 ⁷⁴
Bi ₅ Ti ₃ FeO ₁₅	4	41.04	41.197(1) ⁷¹

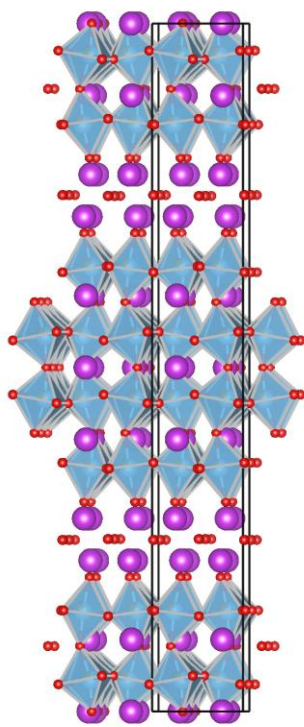


Figure 2.1. a -axis (plus 4°) projection of the $m = 4$ Aurivillius phase $\text{Bi}_5\text{Ti}_3\text{FeO}_{15}$. Drawn using structural parameters from Hervoches *et al.*,⁷⁸ Crystallographica v1.60d⁷⁹ and VESTA 3.0 3D visualization program for crystal structures⁸⁰.

Lomanova *et al.*⁸¹ explored a homologous series of ceramics with general formula $\text{Bi}_{m-1}\text{Fe}_{m-3}\text{Ti}_3\text{O}_{3m+1}$, and demonstrated the existence of structures with m from 4 to 9 using X-ray diffraction and electron probe X-ray microanalysis, including some with fractional m . These compounds were achieved by inserting bismuth ferrite units, BiFeO_3 , into 3-layered bismuth titanate, $\text{Bi}_4\text{Ti}_3\text{O}_{12}$. For this particular homologous series, Lomanova *et al.*⁶⁸ have pointed out that, as the number of perovskite-like layers increases, the cell c parameter rises almost linearly, implying that the perovskite-like units incorporated into the Aurivillius phase structure

experience only slight changes along the c axis with increasing m . An average thickness of the perovskite layers, $p \cong 4.11 \text{ \AA}$ and the fluorite layers, $f \cong 4.08 \text{ \AA}$ was estimated for this series.⁶⁸

Due to the thermodynamic stability curves of the high m -number phases being very similar; there is only a small thermodynamic driving force for any individual m phase. This leads to a tendency for intergrowths of a mixture of different- m intergrowths in bulk-processed Aurivillius phase samples, particularly with increasing m .⁸² Due to the insensitivity of X-ray diffraction to local disorder, this technique is not sufficient to distinguish between large-period superlattices (e.g. $m = 7$) and intergrowths of multiple shorter-period members (e.g. intergrowths of $m = 3$ and $m = 4$).^{83, 84} Therefore, transmission electron microscopy (TEM) is necessary for the confirmation of higher m -number Aurivillius phases.⁸³ Zurbuchen *et al.*⁸⁵ have demonstrated that precise control of temperature and epitaxial growth onto (001) SrTiO_3 has enabled the synthesis of an $m = 8$ $\text{Sr}_5\text{Bi}_4\text{Ti}_8\text{O}_{27}$ phase by pulsed laser deposition (PLD) which is free from intergrowths of other m -phases, as confirmed by both X-ray diffraction and TEM.

The Fe distribution over the two non-equivalent octahedral B cation sites in the perovskite block (classified as B(1) inside the block and B(2) for the octahedra on the outer sides of the block adjacent to the $\text{Bi}_2\text{O}_2^{2-}$ layers) has been investigated for the $\text{Bi}_{m+1}\text{Fe}_{m-3}\text{Ti}_3\text{O}_{3m+3}$ series.⁷² This report has shown that for $m = 3.5$ to 7 , Fe^{3+} ions preferentially occupy the B(1) sites, however the ordered distribution of ions over B(1) and B(2) sites decreases with the increase in the perovskite-like block thickness. At $m \geq 7$, the distribution of Fe^{3+} and Ti^{4+} ions of the perovskite-type block tends to become more random and when the value of m increases up to 8-9, concentrations of ions at B(1) and B(2) sites equalize.⁷²

The Aurivillius phase materials are well known ferroelectrics, with high Curie temperatures ($>500^\circ\text{C}$) and large in-plane spontaneous polarisations.^{62, 86, 87, 88, 89} $\text{SrBi}_2\text{Ta}_2\text{O}_9$

($m = 2$), $\text{SrBi}_2\text{Nb}_x\text{Ta}_{2-x}\text{O}_9$ ($m = 2$) and $\text{Bi}_{3.25}\text{La}_{0.75}\text{Ti}_3\text{O}_{12}$ ($m = 3$) Aurivillius phase materials have been developed for commercial use in Fe-RAM (ferroelectric random access memory) devices.^{90, 91, 92, 93, 94} Interestingly, symmetry differences between structures with even and odd numbers of m means that their ferroelectric properties behave differently, as explained by Newnham et al.⁹⁵ The spontaneous polarization in the Aurivillius phases originates from the rotation and tilt of the BO_6 octahedra in the perovskite block, however, even and odd m -numbered structures rotate differently. At the ferroelectric phase transition, a strong bond is formed between a bismuth ion of the $(\text{Bi}_2\text{O}_2)^{2+}$ layer and an apex oxygen of the perovskite layer, therefore the BO_6 octahedra receive strain energy from the bismuth oxide layer. Strain is minimized in even m -numbered structures by retaining mirror symmetry perpendicular to the c -axis, however retaining the mirror plane perpendicular to the c -axis in the odd m -numbered structures is not energetically favourable as it would result in deformation of the BO_6 octahedral.⁹⁵ The presence of a mirror plane results in cancellation of polarizations along that plane. Thus, even m -numbered Aurivillius phase materials exhibit spontaneous polarization along the a -axis only because of the glide and mirror planes perpendicular to the b - and c -axis, respectively, whereas odd m -numbered phases exhibit minor polarization along the c -axis and major polarisation along the a -axis when the glide planes are perpendicular to the b -axis.⁹⁶ The $(\text{Bi}_2\text{O}_2)^{2+}$ layer is considered to be paraelectric and it is difficult for the bismuth ions to move in the direction of an applied external field. On increasing the number of m -layers, the strain energy that the BO_6 octahedra receive from the bismuth oxide layers decreases and the octahedral cations can move easier toward the direction of the applied electric field. As a result, the saturated coercive field and the minimum electric field for ferroelectric hysteresis loop saturation tends to decrease as m increases.⁹⁷

Given that the layered nature of the Aurivillius phase materials also allows for the incorporation of significant amounts of magnetic ions with +3 to +5 oxidation states⁹⁸ within the $mABO_3$ perovskite units, the normally-conflicting electronic structure requirements for ferroelectricity (unoccupied d orbitals, d^0) and ferromagnetism (partially filled d orbitals, d^n) in a single phase²¹ can potentially be circumvented and the fabrication of single-phase magnetoelectric multiferroic materials could conceivably be accommodated.

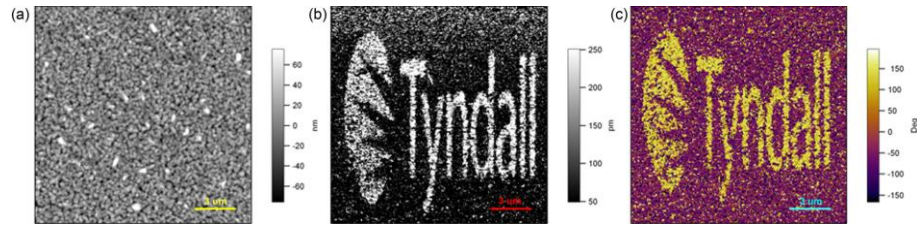


Fig. 2.2. Images of BTF7M3O on SiO₂-Si: (a) topography, (b) out-of-plane PFM (piezoresponse force microscopy) amplitude, and (c) out-of-plane PFM phase after PFM lithography with an applied dc bias of 33.0 V.⁹⁹

Weak room temperature ferromagnetism has been reported for $Bi_{m+1}Fe_{m-3}Ti_3O_{3m+3}$ Aurivillius phases with $m=4$ ¹⁰⁰, and antiferromagnetism (80 to 300K) for $m=6$ ¹⁰¹ and $m=7$ ¹⁰². Ferroelectricity was preserved and fine ferroelectric patterns could be written (**Fig. 2.2**) in manganese-substituted $Bi_5Ti_3Fe_{0.7}Mn_{0.3}O_{15}$ ($m = 4$), however the lack of an appreciable room temperature ferromagnetic hysteresis demonstrates that it is not a room temperature multiferroic.⁹⁹ Zurbuchen *et al.*¹⁰³ revealed that the manganese substituted $Bi_7Mn_{3.75}Ti_{2.25}O_{21}$ (tetragonal with $m=6$) was ferromagnetic below 55K, but not ferroelectric. Ferroelectricity and ferromagnetism above room temperature was reported for cobalt-substituted, 4-layered $Bi_5Ti_3Fe_{0.5}Co_{0.5}O_{15}$ ceramic¹⁰⁴, with a small remanent magnetisation (7.8 memu/g). Subsequent

investigations^{17, 105, 106, 107} of $\text{Bi}_5\text{Ti}_3\text{Fe}_{0.5}\text{Co}_{0.5}\text{O}_{15}$ ceramics and $\text{Bi}_5\text{Ti}_3\text{Fe}_{0.7}\text{Co}_{0.3}\text{O}_{15}$ thin films also displayed ferroelectric and ferromagnetic behaviour at room temperature. However, extensive micro-structural phase analyses detected trace (2 to 3.95 vol.%) levels of $\text{CoFe}_{2-x}\text{Ti}_x\text{O}_4$ second phase inclusions, not observed by X-ray diffraction, but which accounted for the observed magnetization. A remanent magnetisation of 7.8 memu/g as observed by Mao *et al.*¹⁰⁴ would correspond to a trace CoFe_2O_4 second (or impurity) phase level of only 0.03 wt.%, which would be very hard to see by any microanalytical method. Additionally, XAS-PEEM (X-ray absorption spectroscopy photoemission electron microscopy) and XMCD-PEEM (X-ray magnetic circular dichroism photoemission electron microscopy) imaging (**Fig. 2.3**) confirmed that the majority of magnetic response in the $\text{Bi}_5\text{Ti}_3\text{Fe}_{0.7}\text{Co}_{0.3}\text{O}_{15}$ thin film samples arises from the Fe sites of Fe/Co-rich spinel phase inclusions.⁶² While the magnetic contribution from the main phase could not be determined by the XMCD-PEEM images, this data however implies that the $\text{Bi}_5\text{Ti}_3\text{Fe}_{0.7}\text{Co}_{0.3}\text{O}_{15}$ thin films are likely not single phase multiferroics at room temperature. This observation clearly demonstrates the difficulty of explicit assignment of magnetic effects to the parent Aurivillius phase. Other work¹⁰⁸ has reported ferroelectric and ferromagnetic behavior in thin films of $\text{Bi}_{4.15}\text{Nd}_{0.85}\text{Ti}_3\text{Fe}_{0.5}\text{Co}_{0.5}\text{O}_{15}$. Compounds with higher values of m , such as $\text{Bi}_6\text{Ti}_3\text{Fe}_2\text{O}_{18}$ (B6TFO, $m=5$), provide pathways for increasing the proportion of magnetic cations in the Aurivillius phase thin films. For instance, weak ferromagnetic/antiferromagnetic behaviour was reported in rare-earth and Co doped B6TFO^{109, 110, 111, 112} ceramics and thin films, but none of the work presented phase analyses at a level which would exclude the possibility that the ferromagnetic responses were due to trace-level second phases.

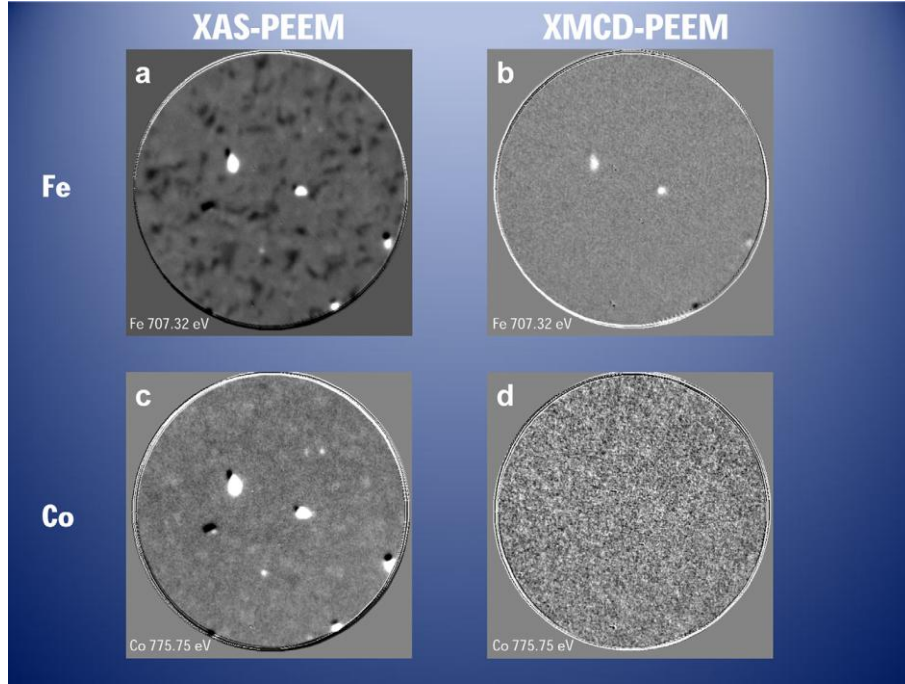


Fig. 2.3. (a) XAS-PEEM image at Fe L-edge resonance (707.32 eV) and (b) XMCD-PEEM image at Fe L-edge resonance (707.32 eV) demonstrating magnetic signature at the Fe edge for the Fe-rich inclusions. (c) XAS-PEEM image at Co L-edge resonance (775.75 eV) and (d) XMCD-PEEM image at Co L-edge resonance (775.75 eV) demonstrating no magnetic signature at the Co edge for the Co-rich inclusions. Frame of view is 6 μm .⁶²

In the proceeding sections, we will summarise how such a higher m an Aurivillius phase material, $\text{Bi}_6\text{Ti}_{2.8}\text{Fe}_{1.52}\text{Mn}_{0.68}\text{O}_{18}$ ($m = 5$)², demonstrates magnetoelectric multiferroicity at room temperature, with a confidence level of 99.5% that the effects are intrinsic to the Aurivillius phase.

21.3. Magnetoelectric Coupling in Multiferroic $\text{Bi}_6\text{Ti}_x\text{Fe}_y\text{Mn}_z\text{O}_{18}$ Systems at Room Temperature

21.3.1 Fabrication and Structural Analysis of $\text{Bi}_{m+1}\text{Ti}_3(\text{Mn/Fe})_{m-3}\text{O}_{3m+1}$ Thin Films

Liquid injection chemical vapour deposition (LI-CVD), sometimes called atomic vapour deposition since its method of operation lies in between that of atomic layer deposition, is an industrially-friendly method for depositing multi-component oxide thin films.¹¹³ This technique allows high gas phase saturation of precursors of low volatility and the growth of multi-component thin films with stoichiometric control at high throughput. Highly oriented and epitaxial thin films of $\text{Bi}_4\text{Ti}_3\text{O}_{12}$ ⁸⁶ and $\text{Bi}_5\text{Ti}_3\text{FeO}_{15}$ ⁸⁹ have been successfully grown by LI-CVD. When designing new materials however, chemical solution deposition methods are often chosen to screen promising compositions since they offer flexibility, control of purity and homogeneous mixing at molecular level with precursors which are generally significantly cheaper than those used for LI-CVD.

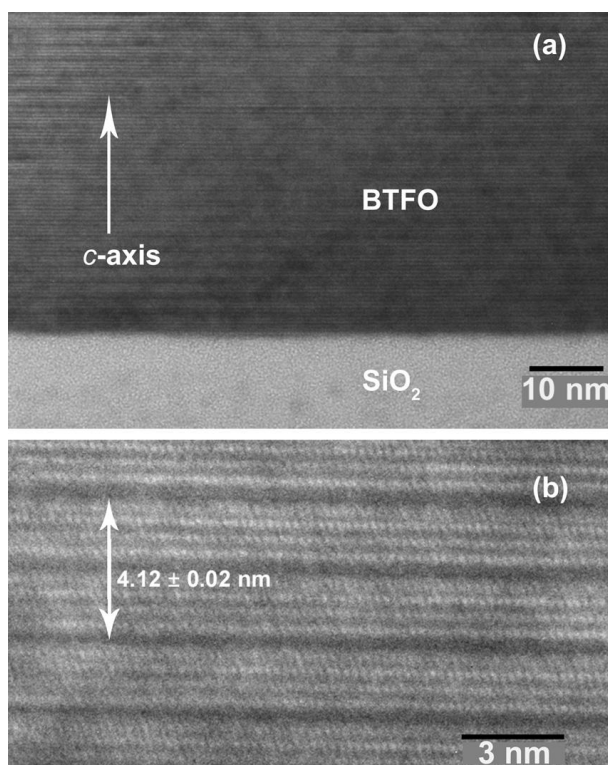


Fig. 3.1.1. (a) TEM image taken from a cross section of the annealed $\text{Bi}_5\text{Ti}_3\text{FeO}_{15}$ film. (b) HRTEM image of the lattice structure.¹¹²

To synthesise thin films of $\text{Bi}_7\text{Ti}_3\text{Fe}_3\text{O}_{21}$ ($m = 6$; B7TFO) and $\text{Bi}_6\text{Ti}_{2.8}\text{Fe}_{1.52}\text{Mn}_{0.68}\text{O}_{18}$ ($m = 5$; B6TFMO)², a chemical solution deposition technique was developed by adapting techniques developed for the $m = 4$ materials $\text{Bi}_5\text{Ti}_3\text{FeO}_{15}$ ⁸⁸, $\text{Bi}_5\text{Ti}_3\text{Fe}_{0.7}\text{Mn}_{0.3}\text{O}_{15}$ ⁹⁹ and $\text{Bi}_5\text{Ti}_3\text{Fe}_{0.7}\text{Co}_{0.3}\text{O}_{15}$ ⁶². Metal salts ($\text{Bi}(\text{NO}_3)_3 \cdot 5\text{H}_2\text{O}$, $\text{Fe}(\text{NO}_3)_3 \cdot 9\text{H}_2\text{O}$) and organometallics ($\text{Ti}(\text{OCH}_2\text{CH}_2\text{CH}_2\text{CH}_3)_4$, $\text{Mn}(\text{C}_5\text{H}_7\text{O}_2)_3$) were used as precursors and lactic acid and acetylacetone acted as solvents to prepare 0.03 mol dm^{-3} solutions of B7TFMO/B6TFMO.² For all solutions, the reactions were conducted at room temperature and 17.5 mol% excess bismuth⁹⁹ was used to compensate for evaporation of bismuth during the annealing process and prevent pyrochlore formation. The films were spin-coated on *c*-plane sapphire substrates by a commercial spinner operating at 1000 rpm for 30 s. Immediately following this, residual organics were removed from the films by

baking on a calibrated hot plate. The spin-coating/baking steps were repeated to achieve desired thicknesses. Films were annealed in ambient air for 1 hour in a conventional furnace at temperatures of 850°C. Final thicknesses of ~100nm and ~200nm were obtained for B7TFO and B6TFMO, respectively, as observed from cross-section HR-SEM (high resolution scanning electron microscopy) measurements.

In fact, *Keeney et al.*² intended to synthesise thin films of $m = 6$ structure only, i.e. $\text{Bi}_7\text{Ti}_3\text{Fe}_3\text{O}_{21}$ ($m = 6$; B7TFO) and $\text{Bi}_7\text{T}_3\text{Fe}_{2.1}\text{Mn}_{0.9}\text{O}_{21}$ ($m = 6$; B7TFMO). The syntheses were carried out under identical conditions; the only difference for the latter sol was that 30% of Fe was replaced by Mn. However, X-ray diffraction (**Fig. 3.1.1.**) and high resolution transmission electron microscopy (HR-TEM) studies revealed that the intended B7TFMO system fitted with a 5-layered B6TFMO system ($a = 5.497$, $b = 5.415$ and $c = 49.280$ Å) with reflections and d -spacings differing to the 6-layered B7TFMO system ($a = 5.468$, $b = 5.472$ and $c = 57.554$ Å). Therefore, inclusion of Mn in the B7TFMO sol has driven the film from an $m = 6$ to an $m = 5$ Aurivillius phase. Multiple HR-SEM energy dispersive x-ray (EDX) surface scans revealed an average film composition of $\text{Bi}_6\text{Ti}_{2.8}\text{Fe}_{1.52}\text{Mn}_{0.68}\text{O}_{18}$, which is slightly deficient in Fe and Mn relative to the sol. It was noted that as a considerable excess of Bi is included in the sol, the minor changes in excess given by producing an $m=5$, rather than an $m=6$ film is not significant. It was also noted that there were no detectable lines from minor phases visible in the XRD patterns of the films. However, the noise level in any XRD scan places a limit on the detectability on such minor phases and the method is intrinsically unable to detect trace levels (typically 1-3 vol %) of strongly magnetic secondary phases which may affect the overall magnetization of the sample.^{61, 62}

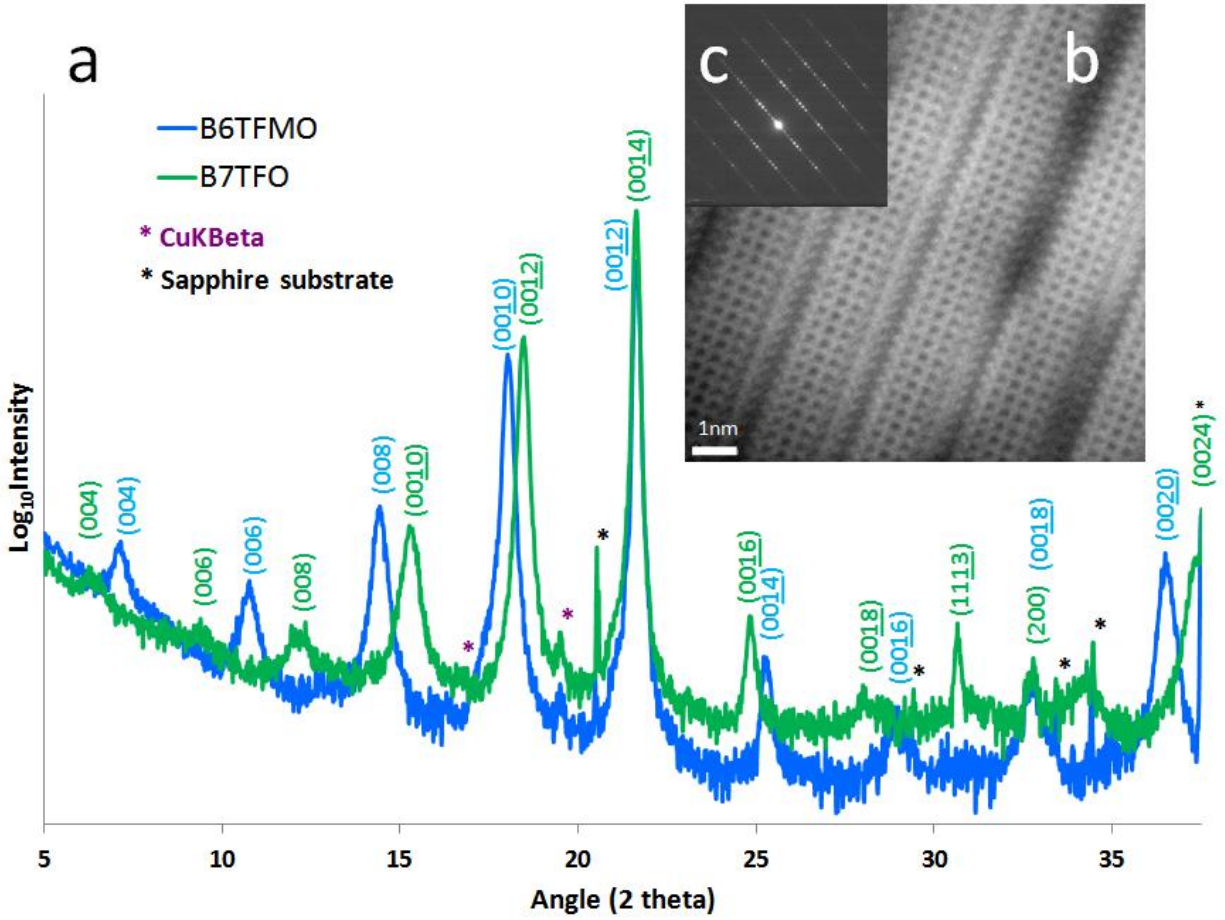


Fig. 3.1.2. (a) XRD patterns from B7TFO and B6TFMO thin films, (b) HR-TEM image and (c) electron diffraction pattern of B6TFMO.²

AFM (atomic force microscopy) and SEM investigations demonstrated that the B7TFO and the B6TFMO thin films crystallised in the typical Aurivillius phase plate-like morphology. 72 hour long HR-SEM-EDX data collection over a $1600\mu\text{m}^2$ area and signals produced maps which showed areas of excess Fe and Mn for the B7TFO and B6TFMO films. In conjunction with detailed cross-sectional HR-TEM/SAED (selected area electron diffraction), these maps showed extremely small amounts (~ 0.01 vol %) of FeO_x oxide inclusions in B7TFO and slightly

larger amounts (~0.1 vol%) of a rock-salt $\text{Mn}_{0.53}\text{Fe}_{0.47}\text{O}$ phase in the B6TFMO. This rock-salt composition is non-ferromagnetic, and antiferromagnetic at low temperatures with a Néel point of ~150K.¹¹⁴ Also visible in these surface HR-SEM-EDX maps were larger areas (~1 μm in diameter; ~1 vol%), similar in shape to the Aurivillius grains, where the Fe content slightly exceeded the surrounding grains. Detailed cross-sectional HR-TEM/SAED and HR-STEM-EDX compositional surveys of these grains showed that they were $m=5$ Aurivillius-structured grains with some $m=6$ intergrowths possessing a higher Fe content than the average of the film composition determined by surface area HR-SEM-EDX. The range of grain compositions spanned both the composition of the sol used in the synthesis ($\text{Bi}_6\text{Ti}_{2.5}\text{Fe}_{1.75}\text{Mn}_{0.75}\text{O}_{18}$) and the average film composition $\text{Bi}_6\text{Ti}_{2.8}\text{Fe}_{1.52}\text{Mn}_{0.68}\text{O}_{18}$ determined by EDX. This microstructural data was important in explaining why a sol which was set-up to deliver an $m=6$ structure could produce an $m=5$ structure without large amounts of second phase appearing in the film.

Note that in order to make up for the deficiency in Ti^{4+} at the *B*-site of $\text{Bi}_6\text{Ti}_{2.8}\text{Fe}_{1.52}\text{Mn}_{0.68}\text{O}_{18}$, the charge balance can only be accommodated by a variable valency in Mn: $\text{Bi}_6\text{Ti}_{2.8}\text{Fe}_{1.52}\text{Mn}^{\text{III}}_{0.48}\text{Mn}^{\text{IV}}_{0.2}\text{O}_{18}$. It was also noted that the content of Mn^{4+} varied within the ~1 vol% Aurivillius phase structures containing increased Fe content. It is believed that this has important consequences for the magnetic properties of the grains,² as will be discussed in Sections 21.3.3 and 21.3.4.

21.3.2 Ferroelectric Investigations of $\text{Bi}_6\text{Ti}_{2.8}\text{Fe}_{1.52}\text{Mn}_{0.68}\text{O}_{18}$ Thin Films

The Aurivillius phase materials are well-known ferroelectrics^{62, 86, 87, 88, 89} where even m -numbered Aurivillius phase materials exhibit spontaneous polarization along the a -axis only, whereas odd m -numbered phases exhibit minor polarization along the c -axis and major polarisation along the a -axis.^{95, 96} $\text{Bi}_6\text{Ti}_3\text{FeO}_{18}$ ceramics have ferroelectric Curie temperatures above 1021K¹¹⁵ and remant polarization of $\sim 9\mu\text{C}/\text{cm}^2$ which has been reported¹¹⁶ to increase to $17.6\mu\text{C}/\text{cm}^2$ on 30% substitution of Fe with Co.

Keeney *et al.*² investigated the local room temperature electromechanical properties of the $\text{Bi}_7\text{Ti}_3\text{Fe}_3\text{O}_{21}$ ($m = 6$; B7TFO) and $\text{Bi}_6\text{Ti}_{2.5}\text{Fe}_{1.75}\text{Mn}_{0.75}\text{O}_{18}$ ($m = 5$; B6TFMO) thin films by using piezoresponse force microscopy (PFM)^{117, 118, 119, 120, 121}. As these films are preferentially c -axis oriented, most of the grains have their crystallographic a -axis lying in the lateral plane of the film. As a result, the single frequency lateral PFM images demonstrate greater piezoresponses (25 pm/V for B7TFO & 19 pm/V for B6TFMO) than the single frequency vertical PFM images (3 pm/V for B7TFO & 8 pm/V for B6TFMO). Given the minor polarization along the c -axis for Aurivillius phases with odd numbers of perovskite layers, the difference between lateral and vertical PFM responses for the B6TFMO ($m = 5$) films is less than that of the B7TFO ($m = 6$) films. In order to amplify the weaker vertical piezoresponse and reduce effects of topography cross-talk, the DART-PFM (Dual AC Resonance Tracking Piezoresponse Force Microscopy) mode was employed (**Fig. 3.2.1**). This method uses the cantilever resonance frequency to boost the piezo signal in the vertical direction, while reducing crosstalk between changes in the sample-tip contact stiffness and the PFM signal by tracking the resonance frequency based on amplitude detection feedback.¹²² Investigations of the local room temperature ferroelectric switching behaviour in the films by vertical DART-PFM switching spectroscopy measurements

in the absence of an applied DC bias demonstrate clear 180° ferroelectric switching for both types of film (**Fig. 3.2.1 (a) to (d)**). Ferroelectric polarization reversal over areas of the B6TFMO film were achieved by applying an applied field of 525 V/ μm vertically to an area of the thin films via the PFM tip (in a “write” step). The written areas could be detected by a subsequent PFM scan (“read” step), (**Fig. 3.2.1 (e) and (f)**). Tests conducted over an 8 hour period demonstrated that the films retained polarization for this period of time.²

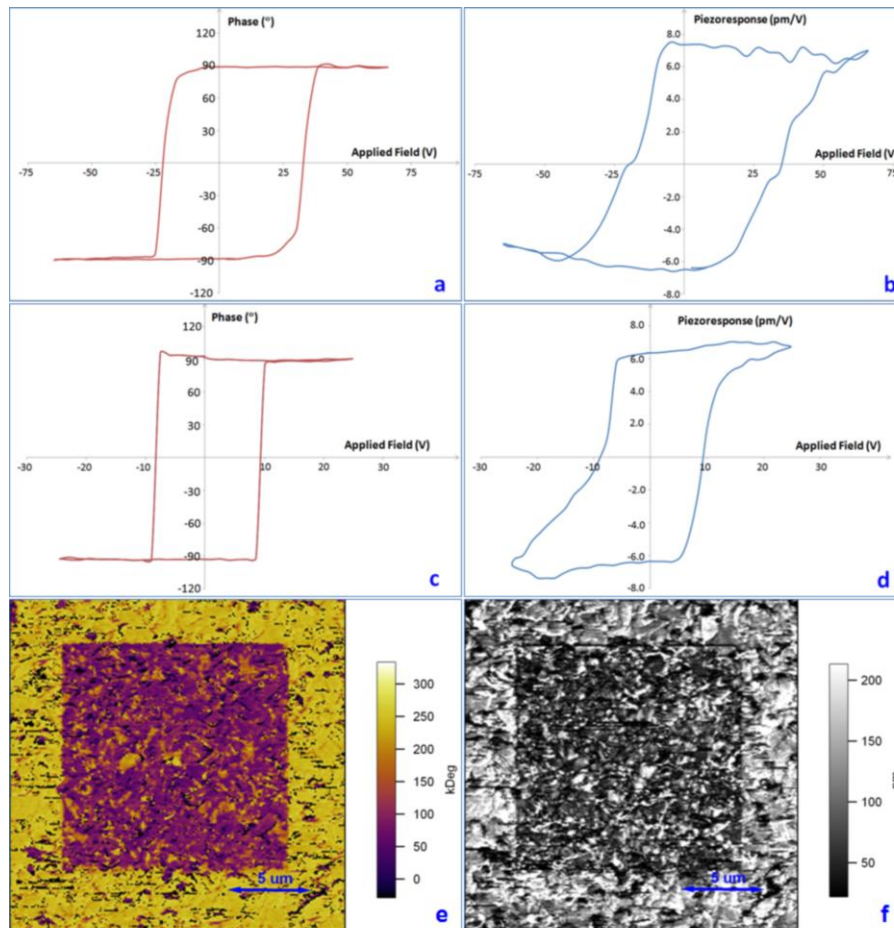


Fig. 3.2.1. Vertical DART-PFM switching spectroscopy **(a)** phase and **(b)** piezoresponse loops of B7TFO and **(c)** phase and **(d)** piezoresponse loops of B6TFMO thin films in the absence of an applied DC bias. Images of B6TFMO on c-plane sapphire: **(e)** out-of-plane PFM phase and **(f)** out-of- plane PFM amplitude after PFM lithography with an applied electric field of 70 V.²

21.3.3 Assessment of Ferromagnetism in $\text{Bi}_6\text{Ti}_{2.8}\text{Fe}_{1.52}\text{Mn}_{0.68}\text{O}_{18}$ Thin Films

Lately the particular class of ferroelectric perovskite compounds $\text{Bi}_2\text{O}_2(\text{A}_{m-1}\text{B}_m\text{O}_{3m+1})$ containing Fe/Co/Mn ions are found to exhibit magnetic behaviour at room temperature which have been reported in several papers.^{101, 102, 123, 124, 125, 126} Ferroelectricity and ferromagnetism above room temperature was reported for the cobalt-substituted, 4-layered $\text{Bi}_5\text{Ti}_3\text{Fe}_{0.5}\text{Co}_{0.5}\text{O}_{15}$ ceramic¹²⁷, with a small remanent magnetisation. Further investigations^{62, 63} of $\text{Bi}_5\text{Ti}_3\text{Fe}_{0.5}\text{Co}_{0.5}\text{O}_{15}$ ceramics and $\text{Bi}_5\text{Ti}_3\text{Fe}_{0.7}\text{Co}_{0.3}\text{O}_{15}$ films also demonstrated ferroelectric and ferromagnetic behavior at room temperature. Subsequently it was observed that Fe/Co-rich spinel phase, likely to be $\text{CoFe}_{2-x}\text{Ti}_x\text{O}_4$, coexist in the film, which accounts for the observed ferromagnetic moment in the films. In a recent study, room temperature ferromagnetic investigations of thin films of Aurivillius phase $\text{Bi}_7\text{Ti}_3\text{Fe}_3\text{O}_{21}$ (B7TFO) and $\text{Bi}_6\text{Ti}_{2.8}\text{Fe}_{1.52}\text{Mn}_{0.68}\text{O}_{18}$ (B6TFMO) was conducted by an intensive magnetometry examination.² The ZFC (zero field cooled)-FC (field cooled) measurement protocol which has been used in this study is a widely used protocol to investigate the magnetic properties as a function of temperature and bias field. From the temperature dependent FC-ZFC magnetization, and remanence curves (**Fig. 3.3.1 (a)**), phase transitions are determined. The point at which splitting between ZFC-FC curves occurs denotes the transition temperatures, for example Néel (T_N) or blocking (T_B) temperatures, below which, the material is antiferromagnetic or ferromagnetic, and result in small or large positive remanences respectively. Another important measurement is the (M-H) measurement, where the magnetization (M) of the sample is measured as a function of applied magnetic field (H) (**Fig. 3.3.1 (b)**). For paramagnetic and diamagnetic materials, the curves obtained are straight lines through the origin with positive and negative slopes respectively. For other types of materials (ferromagnetic/ ferrimagnetic/ antiferromagnetic/ superparamagnetic, etc.) the M-H measurement is non-linear, and takes the

form of the schematic hysteresis loop in **Fig. 3.3.1 (b)**. Other magnetic parameters such as coercivity, remanence, saturation magnetization, etc. help to determine the type of magnetic materials.

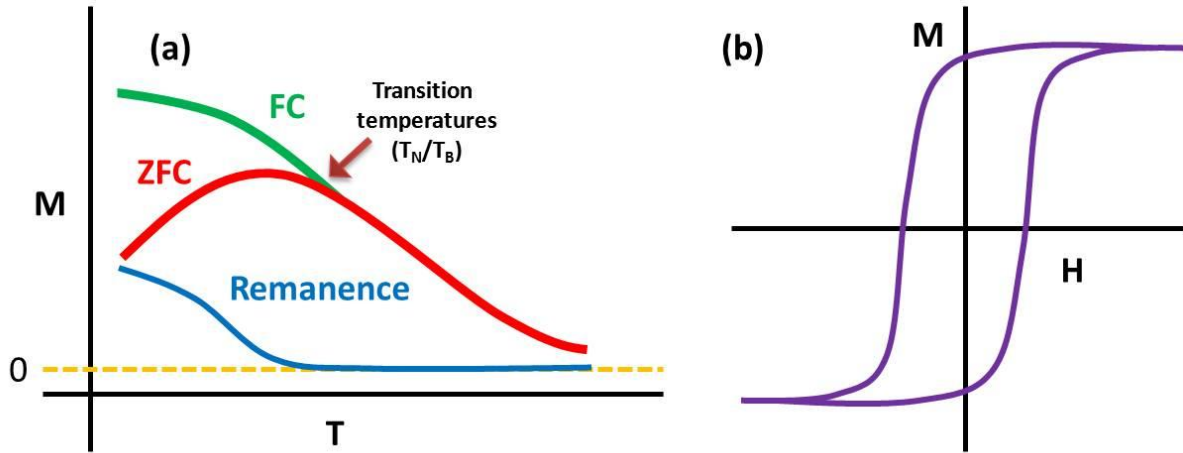


Fig. 3.3.1. Typical Zero Field Cooled (ZFC) – Field Cooled (FC) – Remanence curve **(a)** and magnetic hysteresis (MH) loop **(b)** measured in SQUID magnetometer.²

The magnetic behaviour of the B6TFMO and B7TFO thin films (by L. Keeney *et.al.*²) revealed a strong room temperature ferromagnetic signature for the B6TFMO samples, which was evident from SQUID (superconducting quantum interference device) magnetization measurements as a function of magnetic field (**Fig. 3.3.2 (a)** and **(b)**) and temperature (**Fig. 3.3.2 (c)**), whereas a clear antiferromagnetic behaviour was reported in the case of B7TFO. The geometrical defects of the samples such as roughness and inhomogeneity in sample thickness, (including the fact that 2.44% area of the substrate was not covered by the Aurivillius phase thin film due to pore formation, (inset **Fig. 3.3.2(a)**)) were taken into account for a precise calculation of the magnetic

properties. The calculated saturation magnetization (M_s) measured for Aurivillius phase B6TFMO is reported as 0.74 emu/gm with remanent magnetization (M_r) of 0.022 emu/g (0.18 emu/cm³) and coercivity ($\mu_0 H_c$) of 7mT at 300 K. The coercivity and remanence increased gradually with a decrease in temperature (**Fig. 3.3.2 (d)**). ZFC–FC measurements (**Fig. 3.3.2 (b)**) with a relatively low field of 10 mT were performed to investigate the magnetization behaviour of the B6TFMO sample as a function of temperature. A clear split between the ZFC-FC curves was observed which demonstrates the ferromagnetic nature of the sample since otherwise the ZFC-FC lines would normally coincide¹²⁸ with each other. The compound without Mn substitution, B7TFO ($\text{Bi}_7\text{Ti}_3\text{Fe}_3\text{O}_{21}$), demonstrated an antiferromagnetic Néel temperature at 190 K and a magnetic transition to weak ferromagnetism below 35K (**Fig. 3.3.2 (c)**) as reported previously by A. Srinivas, *et. al.*¹⁰¹ The antiferromagnetic secondary phase $\text{Mn}_{0.53}\text{Fe}_{0.47}\text{O}$ observed in B6TFMO by HR-SEM is reported to have a Néel Temperature at ~150K.¹¹⁴ However no magnetic transition at 150K was detected in the magnetization vs. temperature measurement (MT) for B6TFMO by L. Keeney *et.al.*² Rather, the ZFC-FC curves are well separated below 350K which strengthens the evidence for B6TFMO being ferromagnetic, with a T_C greater than 350K. It was additionally observed that the FC curve of B6TFMO drops down at 190K and increases again sharply below 35K which is similar in nature with the MT behaviour of B7TFO (**Fig. 3.3.2 (c)**). A qualitative explanation of the non-monotonic behaviour of the FC curve for B6TFMO was described.² Most likely, a significant part of the parent B6TFMO phase was modified to become ferromagnetic at the nanoscale, with the remainder being antiferromagnetic in the same way as in the case of unmodified B6TFO^{92, 111, 129, 130}. The variation of magnetization of B6TFMO as a function of temperature (**Fig. 3.3.2 (c)**) was thus

non-monotonic in nature due to the influence of a proportion of grains behaving as it would be expected from the unmodified parent antiferromagnetic B6TFO phase.^{129, 130}

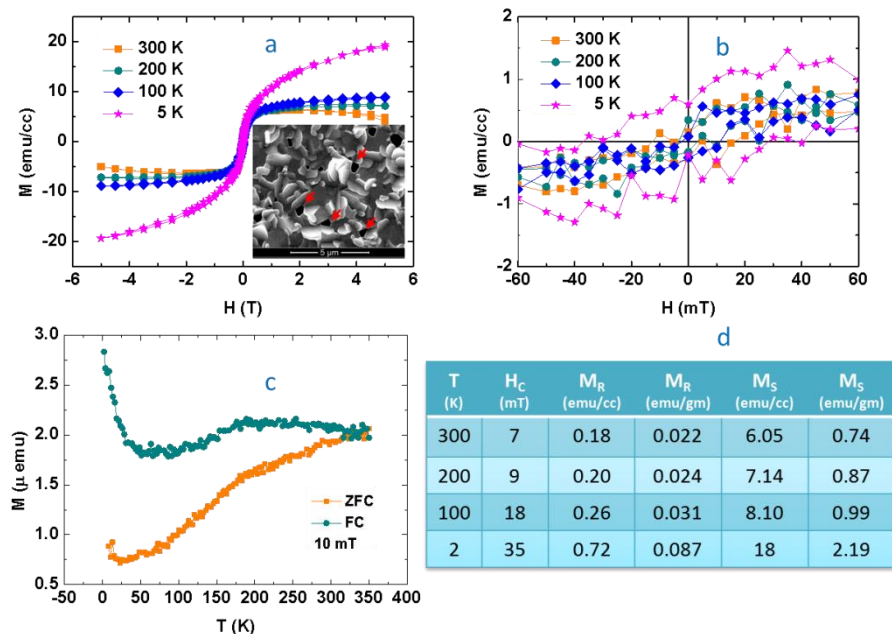


Fig. 3.3.2. The magnetic properties of B7TFO phase were investigated. Figure (a) shows the magnetic hysteresis measured at 2K and the inset shows hysteresis after direct subtraction of the diamagnetic substrate contribution. Figure (b) shows the zoomed hysteresis loop of B6TFMO measured at different temperatures.

In the magnetic hysteresis loop measurement (**Fig. 3.3.2 (a)**), the B6TFMO film shows a saturation magnetization (2.19 emu/gm at 2 K temperature under 5T field) which is substantially higher than the unsubstituted B7TFO phase (0.2 emu/gm at 5 K temperature under 5T field). For antiferromagnetic materials the remanent magnetization is understood to be negligibly small (ideally zero) as the opposite spins cancels out each other. The observation of both high

remanence and a simultaneous increase of remanence and coercivity of B6TFMO with a decrease in temperature strongly support the existence of ferromagnetism in this material.

A possible mechanism for the observed ferromagnetism in B6TFMO can be explained by assuming that there is Mn^{4+} present in the structure which can couple with Fe^{3+} in a ferromagnetic super-exchange interaction via the Goodenough-Kanamori rule:

As a result of a transition metal's coordination geometry, the degeneracy of electronic d orbital states is lifted. This occurs because the electrons in the metal d -orbitals and those in the ligands that the metal ion are coordinated to repel each other due to like charge repulsion. In octahedral symmetry, the 5 d -orbitals split into two sets with an energy difference, Δ_{oct} , where one set, the inter-axial orbitals (t_{2g} orbitals, comprised of d_{xy} , d_{xz} and d_{yz}) are lower in energy than the other set, the axial orbitals (e_g orbitals, comprised of d_z^2 and $d_{x^2-y^2}$) since these are further from the ligand orbitals and therefore experience less repulsion. The size of the gap, Δ_{oct} , between the sets of orbitals depends on various factors including ligand type and the geometry of the complex.

According to the Aufbau Principle, electrons fill lowest available energy levels first, therefore when Δ_{oct} is large, the t_{2g} orbitals are occupied before the e_g orbitals. As such, coordination environments which generate large splitting energies, Δ_{oct} , lead to “low-spin” complexes. Conversely, “high-spin” complexes are formed when there is a sufficiently small Δ_{oct} to obey Hund's rule, which states that if two or more orbitals of equal energy are available, electrons occupy them singly before filling them in pairs. To obey the Pauli Exclusion Principle, when two electrons occupy the same energy level, they must have opposite spin. The electronic arrangement of the 5 d electrons of Fe(III) in both its “low spin” and “high-spin” configurations

is displayed in **Fig. 3.3.3 (a)**. The use of these splitting diagrams can assist in the prediction of the magnetic properties of transition metal complexes.

If orbital degeneracy is lost in a real environment - by chemical bonding or crystal field effects – the orbital contribution to the total magnetic moment is said to be quenched and the spin-only equation can be used to calculate the effective magnetic moment, μ_{eff} (Bohr magneton):

$$\mu_{\text{eff}} = (n(n + 2))^{1/2}$$

where n is the number of unpaired electrons. This relationship holds quite well for first row transition metal ions at room temperature.

For transition metals with 1 to 3 d electrons only the t_{2g} orbitals will be occupied. Therefore, for Mn(IV) μ_{eff} will be 3.87 BM and the e_g orbitals will be empty in all octahedral coordination environments irrespective of the extent of the octahedral splitting energies Δ_{oct} .

The mechanism involving ligand orbitals to facilitate coupling between metal electrons is referred to as super-exchange. According to the Goodenough-Kanamori rule, super-exchange interactions are **antiferromagnetic** where virtual electron transfer is between overlapping orbitals that are each half-filled, for example between the e_g orbitals in high-spin Fe(III). In *antiferromagnetic* materials, adjacent metal ions couple with their spins antiparallel – there are always equal numbers with the two arrangements so that there is no resultant magnetization in the absence of a magnetic field.

On the other hand, the Goodenough-Kanamori rule predicts that super-exchange interactions are strong and **ferromagnetic (Fig. 3.3.3 (b))** when virtual electron transfer is from a half-filled orbital to an empty orbital, for example between a half-filled e_g orbital in high-spin Fe(III) and an empty e_g orbital in low-spin Mn(III) or in Mn(IV) where the e_g orbitals are always

empty regardless of the extent of the octahedral splitting. In *ferromagnetic* materials, the electron spins of each of the atoms couple strongly together to form a resultant unit cell magnetic moment in an applied magnetic field. When the field is then removed, the magnetization does not return to its original value unless heated to the ferromagnetic Curie point temperature.

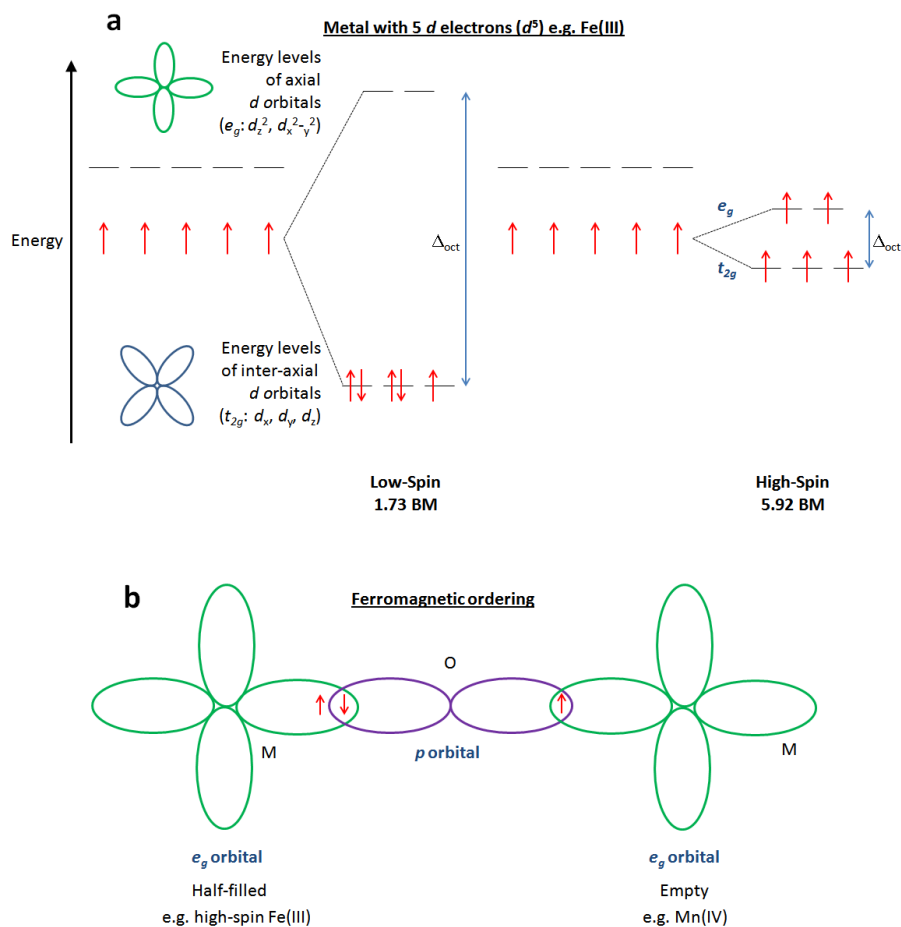


Fig. 3.3.3 (a) Electronic Arrangement of 5 d electrons in “low spin” and “high-spin” configurations and **(b)** mechanism for ferromagnetic ordering.

21.3.4 Room Temperature Magnetoelectric Coupling in $\text{Bi}_6\text{Ti}_{2.8}\text{Fe}_{1.52}\text{Mn}_{0.68}\text{O}_{18}$ Thin Films

Direct evidence of magnetoelectric coupling in the $\text{Bi}_6\text{Ti}_{2.8}\text{Fe}_{1.52}\text{Mn}_{0.68}\text{O}_{18}$ (B6TFMO) thin films was demonstrated by *Keeney et al.*² by performing piezoresponse force microscopy under a variable magnetic field to locally image the coupled piezoelectric-magnetic switching. On application of an in-plane magnetic field of +250 mT during single frequency PFM measurements in the lateral plane (**Fig. 3.4.1**), two situations, (i) piezoelectric domain formation (blue and green circles in the amplitude and phase images) and (ii) piezoelectric domain switching (red and orange circles in the phase images) were observed. Induction of piezoelectric polarization reversal by application of a magnetic field in the positive direction (+250 mT) was also observed by vertical PFM imaging of the out-of-plane piezoresponses (**Fig. 3.4.2 (e), (f)**). When a magnetic field of 250 mT was applied in the opposite (negative) direction, additional areas exhibiting polarization inversion were obtained (**Fig. 3.4.2 (h), (i)**). The switching regions were approximately 250nm in size, clearly related to the Aurivillius grains, of which they were a small fraction of the total number (average change in polarization was 4% for **Fig. 3.4.1** and 7% for **Fig. 3.4.2**) and widely dispersed throughout the film. The fundamental mechanism mediating the magnetoelectric coupling is not obvious from these experiments, however this direct observation of the switching and formation of a ferroelectric polarisation induced by a change in magnetic field within a single phase is significant as it provides strong evidence for the multiferroic character of the B6TFMO thin films. It was proposed that the Aurivillius phase grains that demonstrate magnetoelectric coupling may be those containing the highest levels of Fe/Mn, for which the majority of the Mn will be present as Mn^{4+} .²

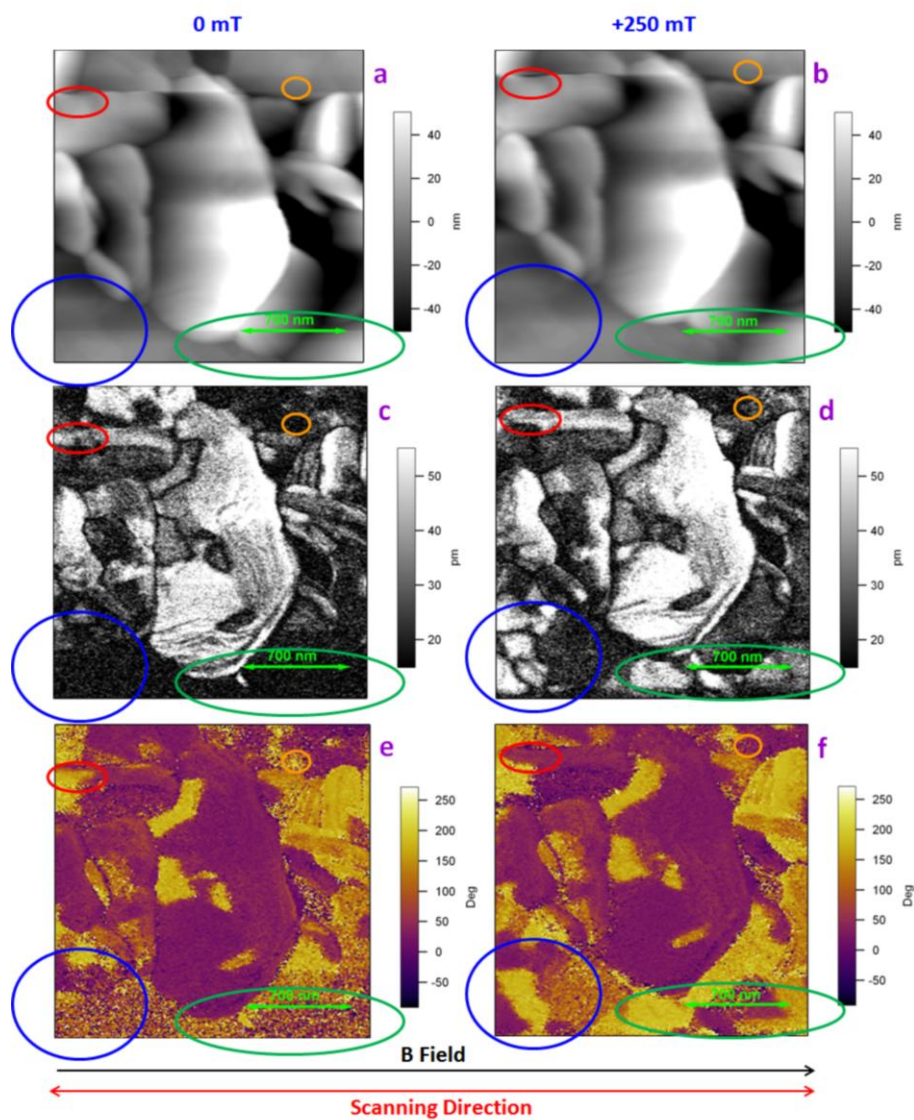


Fig. 3.4.1 Representative images of B6TFMO thin films: (a) topography; (c) lateral PFM amplitude; and (e) lateral PFM phase under 0 mT H field and (b) topography; (d) lateral PFM; and (f) lateral PFM phase under +250 mT H field.²

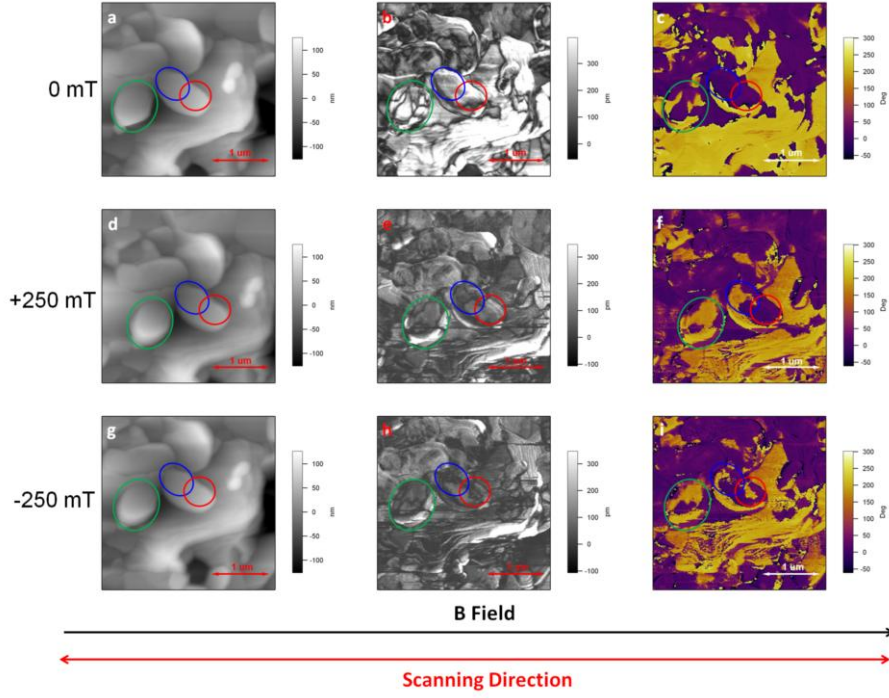


Fig. 3.4.2. Representative images of B6TFMO thin films: (a) topography; (b) vertical PFM amplitude; and (c) vertical PFM phase under 0 mT H field; (d) topography; (e) vertical PFM amplitude; and (f) vertical PFM phase under +250 mT H field; and (g) topography; (h) vertical PFM amplitude; and (i) vertical PFM phase under -250 mT H field.²

21.4 Confidence Level Assessment of Genuine Single Phase Multiferroicity

Per definition, the magnetic properties of a single phase multiferroic material are due to only one phase. It is therefore necessary to exclude the possibility that magnetic effects, for example the remanence magnetization, are caused by the presence of secondary phase of inclusions. In general, it is not practical to scan the whole sample for inclusions, therefore *Keeney et al.*² needed to resort to statistical methods. A statistical approach was developed which only requires a set of measurements at various resolutions to establish an upper limit for the contribution to the remanence magnetization due to the presence of second-phase magnetic inclusions.

In the following we will first review the statistics of a single measurement, and following the introduction of the inclusion size distribution function, a set of measurements is generalized at various resolutions. This then allows the provision of an upper limit for the grain size distribution function and the contribution to the remanence magnetization at a given confidence level.

21.4.1 Statistics of a Single Measurement

In a single measurement, a volume of size V is scanned and the number of inclusions in this volume is detected. In general, this volume will be small compared to the sample size. If in the whole sample, inclusions are present at a volume density ρ and the inclusions are randomly distributed independently of each other, then the probability $P(N)$ of finding precisely N inclusions is given by the Poisson distribution, equation (1):

$$P(N) = \frac{(\rho V)^N}{N!} e^{-\rho V}. \quad (1)$$

This formula also predicts the probability of finding no inclusions as equation (2):

$$P(0) = \exp(-\rho V). \quad (2)$$

This probability decreases exponentially with the scan volume V .

A slightly different situation is now assumed, where ρ (ρ) is not known and in a given scan of a volume V no inclusions are found. Then formula (2) can be used to provide an upper bound for the inclusion density ρ (ρ). For this it is assumed that the event of not finding any inclusions happened with a probability of more than 0.5%, i.e. $P(0) > 0.5\%$. Solving formula

(2) for the inclusion density, and introducing the symbol $\gamma = 1 - 0.5\% = 99.5\%$ for the confidence level, an estimation for the upper bound of ρ (ρ) is obtained as equation (3):

$$\rho < \rho_u = \frac{-\ln(1 - \gamma)}{V} \approx \frac{5.3}{V}, \quad (3)$$

Subject to this confidence level, the ρ_u defined in equation (3) establishes an upper bound for the unknown inclusion density ρ .

21.4.2 The inclusion size distribution function

For a realistic sample, inclusions can be present at various sizes and the volume density might vary with the inclusion size. Therefore an inclusion size distribution function, $p_G(d)$, can be defined such that for small Δd the quantity $p_G(d)\Delta d$ is the density of inclusions with diameters in the interval $[d, d + \Delta d]$. The approach is now generalized from the previous section to the case of a size dependent distribution function. If in a scan of a certain volume V no inclusions are present which are larger than a given minimal detectable size d_m , then the upper bound from equation (3) becomes a constraint on the size distribution function given by equation (4):

$$\int_{d_m}^{\infty} dq p_G(q) < \rho_u \quad (4).$$

21.4.3 Series of measurements at varying resolutions

In practice, the minimal detectable inclusion size decreases with the scan volume. It is therefore often necessary to scan a sample at a number of different resolutions to detect for the presence of inclusions. It is therefore assumed that a number of K scans at different volume sizes V_k and different minimal detectable grain sizes d_k were performed. Here the index k runs from 1 to K starting at large d_k (i.e. $d_k > d_{k+1}$). It is also assumed that there is a physical upper bound $d_0 > d_1$ on the grain size. The probability that no inclusion was detected in measurement

number k is given by $P_k(0)$. If the grain distribution function $p_G(d)$ is known, $P_k(0)$ is given by equation (5):

$$P_k(0) = \exp(-V_k \int_{d_k}^{d_0} dq p_G(q)). \quad (5)$$

It is again assumed that in each individual scan no inclusion larger than the minimal inclusion size, d_k was found. The probability for this zero outcome is given by the product of the probability for not detecting inclusions over all scans, i.e.

$$P(0) = P_1(0)P_2(0) \cdots P_{N_m}(0).$$

Using equation (5), it then follows that the condition in equation (6):

$$V_{N_m} \int_{d_K}^{d_{K-1}} dq p_G(q) + (V_K + V_{K-1}) \int_{d_{K-1}}^{d_{K-2}} dq p_G(q) + \quad (6)$$

$$\dots + \left(\sum_{k=1}^K V_k \right) \int_{d_1}^{d_0} dq p_G(q) < -\ln(1 - \gamma) \approx 5.3$$

holds with a confidence level of $\gamma = 99.5\%$. Equation (6) gives us an estimate of the upper limit of the grain size distribution function $p_G(d)$ integrated over grain size intervals from d_k to d_{k-1} . In practice, observable quantities (for example the remanence) are more naturally connected to the volume fractions of the inclusions at certain grain sizes. This motivates the rewriting of equation (6) using volume fractions.

If it is assumed for simplicity that the inclusions are spherical, then the volume fraction φ_k of inclusions between sizes d_k and d_{k-1} can be calculated from the grain size distribution $p_G(d)$ via

$$\varphi_k = \int_{d_k}^{d_{k-1}} dq p_G(q) \frac{4}{3} \pi \left(\frac{q}{2}\right)^3 \leq \left[\int_{d_k}^{d_{k-1}} dq p_G(q) \right] \frac{\pi}{6} d_{k-1}^3.$$

In the last step the worst case scenario is employed in that the weight of the grain distribution function is located at the large inclusion sizes. Using this inequality in equation (6) yields a convenient upper limit for the allowed volume fractions,

$$V_K \frac{\varphi_K}{d_{K-1}^3} + \left(\sum_{k=K}^{K-1} V_k \right) \frac{\varphi_{K-1}}{d_{K-2}^3} + \dots + \left(\sum_{k=K}^1 V_k \right) \frac{\varphi_1}{d_0^3} \quad (7)$$

$$< -\frac{\pi}{6} \ln(1 - \gamma) \quad \approx \quad 2.8 \quad (8)$$

which again holds with a confidence level of γ . It therefore follows that there is an upper limit on the volume fraction φ_k of inclusions with diameter in the interval $[d_k, d_{k-1}]$ given by

$$\varphi_k < \frac{-d_{k-1}^3}{\sum_{j=K}^k V_j} \frac{\pi}{6} \ln(1 - \gamma) \approx 2.8 \frac{d_{k-1}^3}{\sum_{j=K}^k V_j}. \quad (9)$$

21.4.4 Upper limit on the contribution to remanent magnetization

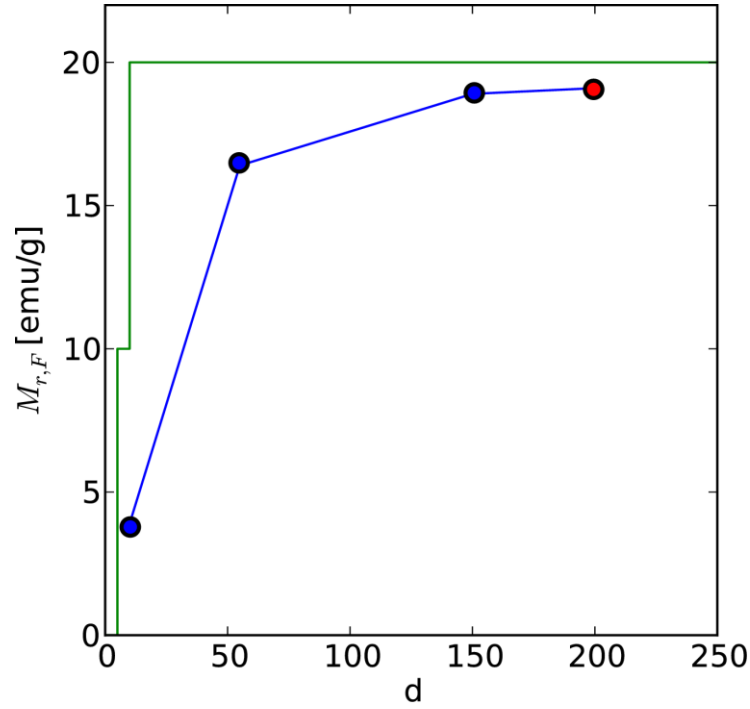


Fig. 4.1. Remanent magnetization $M_{r,F}$ of Fe_3O_4 as function of grain size. The blue line shows literature data from ¹³¹ (blue dots) and ¹³² (red dot). Because there are only a few literature values, a conveniently chosen (piecewise constant) green line is chosen which is assumed to conservatively overestimate (up to the chosen confidence level) the true remanent magnetization for all grain sizes d .

So far it has been discussed how the absence of inclusions in a number of volume scans at various resolutions limits the possible inclusion size distribution function $p_g(d)$. In many applications however, this quantity is not in itself of primary interest, but a possible physical effect caused by the inclusions. In *Keeney et al.*'s case the physical quantity of interest is the

magnetic remanence, and the aim was to find an upper bound for the contribution of undetected inclusions to this quantity.² Using the upper bound estimates for the volume fractions φ_k given in equation (9), the maximal contribution to the remanence from inclusions with diameters in the interval $[d_k, d_{k-1}]$ is given by equation (10):

$$M_{r,k} = \frac{-d_{k-1}^3}{\sum_{j=N_m}^k V_j} \frac{\pi}{6} \ln(1 - \gamma) M_{r,F}(d_{k-1}) \quad (10)$$

Here $M_{r,F}(d)$ is the remanence magnetization of pure Fe_3O_4 grains of diameter d . The literature^{131, 132} values for this function are plotted in **Fig. 4.1**. For simplicity it is assumed that $M_{r,F}(d)$ vanishes for $< 5nm$. Furthermore $M_{r,F}(d) = 10emu / g$ is set for $5nm < d < 10nm$ and $M_{r,F}(d) = 20emu / g$ for $d > 20nm$ which are conservative estimates as shown in figure

Fig. 4.1.

The total contribution from inclusions to the remanent magnetization is then simply given as a sum over the contributions from the individual size intervals:

$$M_r = \sum_{k=1}^K W_k M_{r,k}.$$

Because of equations (7) and (10) the parameters W_1, \dots, W_K fulfill the constraint

$$\sum_{k=1}^K W_k = 1$$

with a confidence level γ . Therefore it can be concluded that the contribution to the magnetization remanence from inclusions M_r has an upper bound

$$M_r \leq \max_{k=1 \dots K} \{M_{r,k}\}$$

with confidence $\gamma = 99.5\%$. From the analysis by *Keeney et al.*,² it was concluded that the contribution to the remanence in the B6TFMO ($\text{Bi}_6\text{Ti}_{2.8}\text{Fe}_{1.52}\text{Mn}_{0.68}\text{O}_{18}$) thin films from unobserved magnetic inclusions is less than 2.8 memu/g with a confidence level better than 99.5%.

21.5 Potential devices / applications based on single phase magnetoelectric multiferroics

The semiconductor technology industry has provided remarkable developments in computer processing speeds and miniaturisation since Moore's prediction in 1965¹³³ and has had a dramatic impacts on our lives. However, for future advances in miniaturisation, the memory capacity of digital devices will also need to improve at exponential rates. The development of an ideal energy-efficient non-volatile memory having the potential to retain high densities of data in the absence of power or an external stimuli¹³⁴ is still an elusive goal. The most common primary memory used in computers and electronic devices today is dynamic access memory (DRAM), which is a volatile memory allowing each bit of data to be stored in a separate capacitor and accessed at clock cycle times in the order of nano-seconds. However, the data is lost quickly when the power is removed; therefore information must be transferred to a secondary memory, such as a non-volatile magnetic hard drive. Examples of other non-volatile memory devices include EEPROM (Electrically Erasable Programmable Read-Only Memory) and flash type memory. However, both of these memories suffer from limited life-spans, increased write times and production costs.¹³⁵

In the 1970s, Esaki¹³⁶ proposed that ferroelectric materials could be ideal candidate for use in non-volatile data storage devices (ferroelectric random access memory (FeRAM)) by taking advantage of their two spontaneously switchable polarization states.¹³⁷ Among the known ferroelectric materials, the solid solution $\text{PbZrO}_3\text{--PbTiO}_3$ (PZT) and Aurivillius phase $\text{SrBi}_2\text{Ta}_2\text{O}_9$ (SBT) have been developed for FeRAM applications. Both these materials demonstrate some drawbacks which restrict their applications however, such as PZT exhibits polarization fatigue, while in the case of $\text{SrBi}_2\text{Ta}_2\text{O}_9$ (SBT), the high processing temperatures required makes them difficult to process in conjunction with functional silicon technologies.¹³⁸

In addition, FeRAM has number of technical drawbacks which restricts their full fledged production in the memory technology industry. Firstly, the data read-out is performed by measuring the net flow of transient current during charge polarization reversal across the circuit. This implies that read out step is destructive in FeRAM.¹³⁹ Secondly, FeRAM based devices function by charge sensing and when the lateral size of the ferroelectric capacitor is reduced to the sub-micron scale, the stored charges tend to be very small and beyond detectability limits.¹³⁴

An alternative to a non-volatile memory with the destructive data read-out of FeRAM is magnetic random access memory (MRAM). MRAMs equal or surpass alternative non-volatile memory technologies in terms of access time and endurance,^{3, 4} however, a current drawback of these devices in obtaining a competitive cost/bit is the considerable power that is usually required for magnetic writing. Energy-efficient approaches to reduce the write energy have received much focus recently. One way is to reverse the stored magnetisation by spin transfer, employing spin polarization current rather than an external magnetic field. Another way that write-energy could be significantly decreased is by using a write-scheme which relies on applied voltage rather than current. The ability to control the direction of magnetization in a ferromagnetic layer by purely electrical means would overcome the current requirement of high current densities in spin-transfer torque MRAM and offer **low-power approaches** for spin-based information control. A relatively simple device to demonstrate electric field control of ferromagnetism was shown by Chu *et al.*¹⁴⁰ The device (**Fig. 5.1.**) consists of in-plane electrodes that enable the application of in-plane electric fields to the BiFeO₃ layer which in-turn changes the magnetic state of the CoFe ferromagnetic top layer.

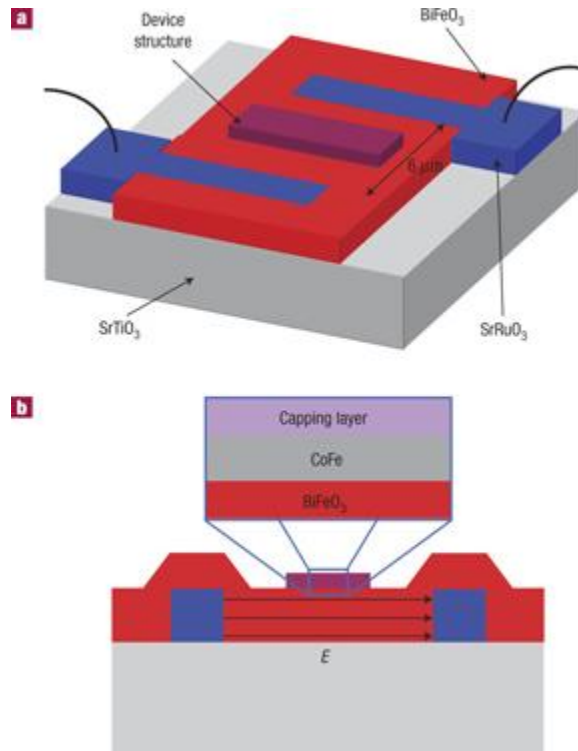


Fig. 5.1. Dynamic switching device structure. Three dimensional (a) and cross-sectional (b) schematic diagram of the co-planar epitaxial electrode device showing a structure that could enable controlled ferroelectric switching and electrical control of ferromagnetism.¹⁴⁰

Hence, miniaturisation and feature scaling, increased density and processing speeds, non-volatility and decreased power dissipation are major challenges to overcome in the creation of a universal memory which can scale beyond the current state-of-the art. These physical requirements are potentially achievable by incorporating multi-state logic in a memory cell which can be electrically written and magnetically read (or *vice versa*) in the form of multiferroic magnetoelectric (ME) logic memory. With strong magnetoelectric coupling between the ferroelectric and ferromagnetic states however, the four available switching states $(+P, +M)$, $(+P, -M)$, $(-P, +M)$ and $(-P, -M)$, where P represents the polarization state and M represents the

magnetization state, are not absolutely independent of each other¹⁴¹ and the only combinations that are independently achievable are either $(+P, +M)$ and $(-P, -M)$ or $(+P, -M)$ and $(-P, +M)$, which of course is not a 4-state memory. This problem can be circumvented by forming a ferromagnetic-magnetoelectric tunnel junction, where combination of electroresistance and magnetoresistance can result in four state memory effect.⁵

Multiferroic tunnel junctions (MFTJs) (**Fig. 5.2.**) consist of two asymmetric oxide and/or metal electrodes separated by an **ultra-thin multiferroic** barrier layer. The approach exploits the tunnelling of electrons through an **ultra-thin** (< 10 nm) multiferroic thin film, providing ***giant electroresistance/magnetoresistance*** effects and a means for non-destructive read-out of non-volatile memory states with increased **storage densities** and **data rates** with low-power electrical write operation.^{5, 142} Recent investigations of ferroelectric oxide thin films have demonstrated that ferroelectricity can persist down to the **nanometre scale**¹⁴³ and therefore can function as ultra-thin barriers for tunnel junctions. Depending on the direction of the remanent polarization in the ferroelectric, charges are accumulated or depleted in the barrier layer, which influences its electroresistance (ER). Resistive memories can be read more simply than ferroelectric capacitors (where the polarization is read by an applied voltage) by monitoring the source-drain current in a field-effect transistor. If the barrier layer can also act as a ferromagnet, as in the case of single-phase multiferroic materials, the ferromagnetic barrier layer can yield different tunnel barrier heights for spin-up and spin-down electrons. Magnetization may be easily readout from resistance measurements as is done for magnetic tunnel junctions. Non-polarized electrons from a non-magnetic metal crossing a ferromagnetic-multiferroic barrier will be transmitted differently depending on their spin, thereby acquiring a finite spin polarization, which is referred to as spin-filtering. If a half-metallic ferromagnetic counter electrode is added,

aligning its magnetization parallel or antiparallel to that of the barrier yields different resistance levels, where the magnitude of the tunnel magnetoresistance (TMR) is larger for antiparallel arrangements.¹⁴⁴

Ferroelectricity and ferromagnetism has been shown to persist down to a thickness on 2 nm in the single-phase multiferroic $\text{La}_{0.1}\text{Bi}_{0.9}\text{MnO}_3$.⁵ A large TMR (90%) and an ER of 22% has been obtained at a 2V bias operation in a four-resistance-state MTFJ system using this material as a barrier separating $\text{La}_{0.66}\text{Sr}_{0.33}\text{MnO}_3$ and SrTiO_3 electrodes; however these results were obtained at very low temperature (4 K), requiring liquid helium cooling. The search for an ultra-thin room-temperature multiferroic remains before a 4-state-logic device based on MTFJs is practically useful.¹⁴⁵ The B6TFMO Aurivillius phase is therefore an ideal candidate for testing the feasibility of a MFTJ functional at room temperature based on a single-phase multiferroic barrier layer.

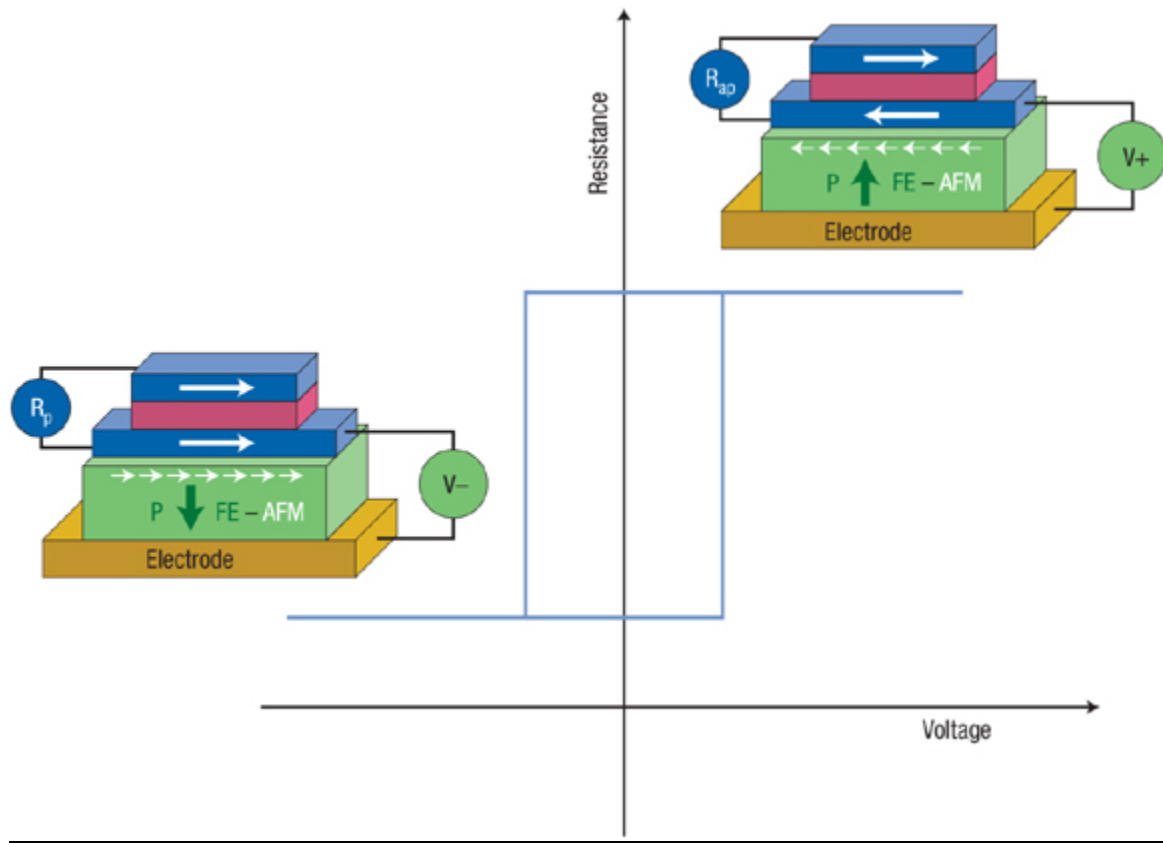


Fig. 5.2. The binary information is stored by the magnetization direction of the bottom ferromagnetic layer (blue), read by the resistance of the magnetic trilayer (R_p when the magnetizations of the two ferromagnetic layers are parallel), and written by applying a voltage across the multiferroic ferroelectric antiferromagnetic layer (FE-AFM; green). If the magnetization of the bottom ferromagnetic layer is coupled to the spins in the multiferroic (small white arrows) and if the magnetoelectric coupling is strong enough, reversing the ferroelectric polarization P in the multiferroic changes the magnetic configuration in the trilayer from parallel to antiparallel, and the resistance from R_p to antiparallel (R_{ap}). A hysteretic dependence of the device resistance with voltage is achieved (blue curve).¹³⁹

Another application of multiferroic materials is in the fabrication of magnetic field sensors. Magnetic sensors have been used in analysing and controlling various functions for many decades. The high storage capacity of computers is due to the use of magnetic sensors in magnetic storage disks and tape drives. Aeroplanes fly with improved safety standards due to the increased reliability of non-contact switching with magnetic sensors¹³⁰. Magnetic field sensors have other numerous applications which include automotive sensors, navigation systems, non-destructive material testing, security systems, structural stability, medical sensors, and military instruments. These numerous applications have led to great deal of research in improving upon the current magnetic sensors. There are various ways of preparing magnetic sensors including fabrication by exploiting various effects such as Faraday's induction law, the Hall Effect, the magneto-resistive effect and using magnetic tunnel junctions. A comprehensive review is provided by James Lenz and Alan S. Edelstein¹³¹ for further reading.

In most of the magnetic field sensors, the basic principle of change in the electrical properties of a material on application of a magnetic field can be exploited¹³¹. The magnetoelectric multiferroic coupling between two materials can also be used to fabricate magnetic field sensors. This multiferroic coupling can be exploited in two different ways. The first method uses composites made from piezoelectric and magneto-strictive materials. Two different layers of magneto-strictive and piezoelectric materials are glued together with a binder. A magneto-strictive material such as NiFe_2O_4 ¹³², or alloys, e.g. TbDyFe_2 (Terfenol-D)^{133, 134} is glued with a binder to a piezoelectric material with a high piezoelectric coefficient such as $\text{Pb}(\text{Zr,Ti})\text{O}_3$ (PZT)¹³⁰. The application of a magnetic field will create a strain in magneto-strictive layer which in turns will be transferred to the piezoelectric material. The binder plays an important role as it helps in transferring the strain from one material to another.

The second method is by using single phase multiferroics showing magnetoelectric switching. These kinds of sensors work on the principle of linear coupling between magnetic and electrical orders. **Fig. 5.3.** shows the structure of a possible magnetic field sensor.

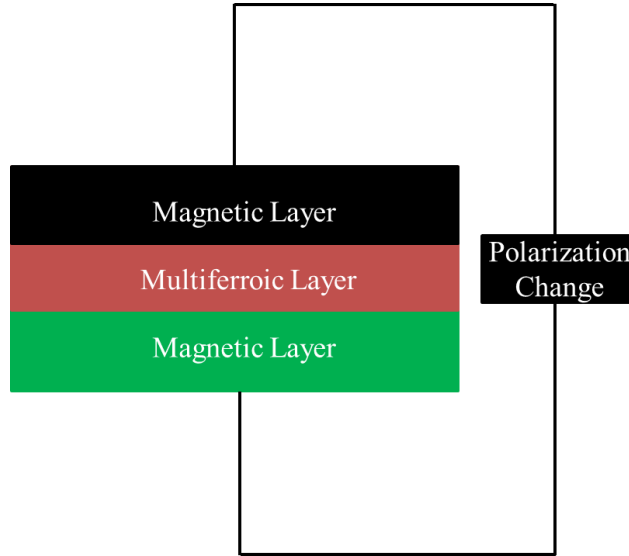


Fig. 5.3. Image of a possible single-phase multiferroic magnetic field sensor where the multiferroic material is sandwiched in between two magnetic electrode layers.

This magnetic field sensor consists of a tri-layer structure where the multiferroic material is sandwiched between two magnetic electrodes (**Fig. 5.3.**). Any change near the vicinity of the magnetic layer will change the magnetization in multiferroic layer. Since there is a coupling between magnetic and electric orders, this change in magnetization will change the polarization values in the multiferroic layer with standard circuitry. The only requirement for this kind of device is strong magnetoelectric coupling in single phase multiferroic material which is usually hard to achieve at room temperature. However, recent work on $\text{Bi}_6\text{Ti}_{2.8}\text{Fe}_{1.52}\text{Mn}_{0.68}\text{O}_{18}$ (B6TFMO) demonstrated multiferroic magnetoelectric coupling which in principle could be used

to prepare future magnetic field sensors. The use of a single phase multiferroic material has an added advantage of faster response times due to the direct coupling between the ferroic order parameters. Fabrication of single phase sensors is a less complex process without the need for a binder layer to couple piezoelectric and magneto-strictive materials. The need for lead-based materials with high piezoelectric coefficient such as PZT, for composite sensors, should be replaced with less toxic and more environmentally-friendly substitutes. Single phase materials such as B6TFMO, based on bismuth based systems, are good candidates for fabrication of future magnetic field sensors and can provide less toxic way of preparing magnetic-based sensing devices.

21.6 Summary and conclusions

By inserting magnetic ions into layered-structured ferroelectric materials in the Aurivillius phase, *Keeney et al.*² were successful in synthesising thin films of average composition, $\text{Bi}_6\text{Ti}_{2.8}\text{Fe}_{1.52}\text{Mn}_{0.68}\text{O}_{18}$ (B6TFMO), which demonstrate ferroelectric and ferromagnetic properties at room temperature. Direct evidence of magnetoelectric coupling was demonstrated by performing piezoresponse force microscopy (PFM) under a variable magnetic field, whereupon magnetic-field-induced ferroelectric domain switching and formation was demonstrated under application of modest (± 250 mT) magnetic fields. Although no spinel impurity phases visible in the XRD patterns, a thorough microstructural phase analysis performed on the films to investigate whether trace levels of ferromagnetic spinel inclusions could be responsible for the observed ferromagnetism in B6TFMO. This detailed analysis demonstrated no evidence for ferromagnetic impurity inclusions above the detection level of the experiments (0.01 vol.%). Statistical analysis based on the volumes inspected placed a confidence of 99.5% that the observed ferromagnetism was not coming from unobserved/undetected ferromagnetic spinel grains. This analysis, coupled with the direct observation of the switching and formation of a ferroelectric polarisation induced by a change in magnetic field within a single phase, is significant as it provides strong evidence that that B6TFMO thin films are single-phase ferroelectric ferromagnetic magnetoelectric multiferroics at room temperature. The body of evidence reported indicates that the origin for the ferromagnetism/magnetoelectric coupling arises from Aurivillius phase grains containing higher $\text{Fe}^{3+}/\text{Mn}^{4+}$ content; however this remains to be verified. The fundamental mechanism for how the ferroelectric and magnetic order parameters are coupled also remains to be understood. The study by *Keeney et al.*² demonstrate that with materials development and design, the

development of room temperature multiferroic materials can be achieved and that the B6TFMO thin films are exciting candidates for potential use in multiferroic, magnetoelectric logic devices that could potentially meet future industry requirements in energy efficient, high density memory applications.

21.7 References

1. L. W. Martin, S. P. Crane, Y. H. Chu, M. B. Holcomb, M. Gajek, M. Huijben, C. H. Yang, N. Balke, and R. Ramesh, "Multiferroics and magnetoelectrics: thin films and nanostructures," *J. Phys.-Condens. Matter*, 20 434220 (2008).
2. L. Keeney, T. Maity, M. Schmidt, A. Amann, N. Deepak, N. Petkov, S. Roy, M. E. Pemble, and R. W. Whatmore, "Magnetic-Field-Induced Ferroelectric Switching in Multiferroic Aurivillius Phase Thin Films at Room Temperature," *Journal of the American Ceramic Society*, 96[8] 2339-57 (2013).
3. "Assessment of the Potential and Maturity of Selected Emerging Research Memory Technologies Workshop & ERD (Emerging Research Devices) /ERM Working Group Meeting (April 6-7 2010)," (2010).
4. "Emerging Research Materials, INTERNATIONAL TECHNOLOGY ROADMAP FOR SEMICONDUCTORS, 2009 Edition," (2009).
5. M. Gajek, M. Bibes, S. Fusil, K. Bouzehouane, J. Fontcuberta, A. Barthelémy, and A. Fert, "Tunnel junctions with multiferroic barriers," *Nat Mater*, 6[4] 296-302 (2007).
6. N. A. Hill, "Why Are There so Few Magnetic Ferroelectrics?," *J. Phys. Chem. B*, 104[29] 6694-709 (2000).
7. M. Schmidt, A. Amann, L. Keeney, M. E. Pemble, J. D. Holmes, N. Petkov, and R. W. Whatmore, "Absence of Evidence \neq Evidence of Absence: Statistical Analysis of Inclusions in Multiferroic Thin Films," *Submitted* (2014).
8. V. J. Folen, G. T. Rado, and E. W. Stalder, "Anisotropy of the Magnetoelectric Effect in Cr_2O_3 ," *Phys. Rev. Lett.*, 6[11] 607-08 (1961).

9. T. H. E. Lahtinen, K. J. A. Franke, and S. van Dijken, "Electric-field control of magnetic domain wall motion and local magnetization reversal," *Sci. Rep.*, 2 258 (2012).
10. T. Kimura, Y. Sekio, H. Nakamura, T. Siegrist, and A. P. Ramirez, "Cupric oxide as an induced-multiferroic with high-TC," *Nat. Mater.*, 7[4] 291-94 (2008).
11. T. Kimura, T. Goto, H. Shintani, K. Ishizaka, T. Arima, and Y. Tokura, "Magnetic control of ferroelectric polarization," *Nature*, 426[6962] 55-58 (2003).
12. E. Ascher, H. Rieder, H. Schmid, and H. Stossel, "Some Properties of Ferromagnetoelectric Nickel-Iodine Boracite, $\text{Ni}_3\text{B}_7\text{O}_{13}\text{I}$," *J. Appl. Phys.*, 37[3] 1404-05 (1966).
13. D. Higashiyama, S. Miyasaka, N. Kida, T. Arima, and Y. Tokura, "Control of the ferroelectric properties of DyMn_2O_5 by magnetic fields," *Phys. Rev. B*, 70[17] 174405 (2004).
14. J. Ryu, S. Priya, A. V. Carazo, K. Uchino, and H.-E. Kim, "Effect of the Magnetostrictive Layer on Magnetoelectric Properties in Lead Zirconate Titanate/Terfenol-D Laminate Composites," *J. Am. Ceram. Soc.*, 84[12] 2905-08 (2001).
15. F. Zavaliche, T. Zhao, H. Zheng, F. Straub, M. P. Cruz, P. L. Yang, D. Hao, and R. Ramesh, "Electrically Assisted Magnetic Recording in Multiferroic Nanostructures," *Nano Lett.*, 7[6] 1586-90 (2007).
16. J. Hutchby and M. Garner, *Assessment of the Potential & Maturity of Selected Emerging Research Memory Technologies Workshop & ERD/ERM Working Group Meeting (April 6-7, 2010)* (2010).
17. L. W. Martin, S. P. Crane, Y. H. Chu, M. B. Holcomb, M. Gajek, M. Huijben, C. H. Yang, N. Balke, and R. Ramesh, "Multiferroics and magnetoelectrics: thin films and nanostructures," *J. Phys.-Condes. Matter*, 20 434220 (2008).

18. P. Borisov and W. Kleemann, "Exchange bias and ferromagnetic coercivity in heterostructures with antiferromagnetic Cr_2O_3 ," *Journal of Applied Physics*, 110[3] 033917 (2011).
19. J.-B. Li, Y. P. Huang, G. H. Rao, G. Y. Liu, J. Luo, J. R. Chen, and J. K. Liang, "Ferroelectric transition of Aurivillius compounds $\text{Bi}_5\text{Ti}_3\text{FeO}_{15}$ and $\text{Bi}_6\text{Ti}_3\text{Fe}_2\text{O}_{18}$," *Applied Physics Letters*, 96[22] 222903 (2010).
20. G. D. Christian, "Analytical Chemistry," Fifth ed. John Wiley and Sons, Inc., (1994).
21. N. A. Hill, "Why Are There so Few Magnetic Ferroelectrics?," *Journal of Physical Chemistry B*, 104[29] 6694-709 (2000).
22. L. W. Martin and D. G. Schlom, "Advanced synthesis techniques and routes to new single-phase multiferroics," *Current Opinion in Solid State & Materials Science*, 16[5] 199-215 (2012).
23. R. Ramesh, "Materials science: Emerging routes to multiferroics," *Nature*, 461[7268] 1218-19 (2009).
24. R. Ramesh and N. A. Spaldin, "Multiferroics: progress and prospects in thin films," *Nat Mater*, 6[1] 21-29 (2007).
25. L. W. Martin, Y. H. Chu, and R. Ramesh, "Advances in the growth and characterization of magnetic, ferroelectric, and multiferroic oxide thin films," *Materials Science and Engineering: R: Reports*, 68[4-6] 89-133 (2010).
26. Y. H. Chu, M. P. Cruz, C. H. Yang, L. W. Martin, P. L. Yang, J. X. Zhang, K. Lee, P. Yu, L. Q. Chen, and R. Ramesh, "Domain Control in Multiferroic BiFeO_3 through Substrate Vicinality," *Advanced Materials*, 19[18] 2662-66 (2007).

27. D. Sando, A. Agbelele, D. Rahmedov, J. Liu, P. Rovillain, C. Toulouse, I. C. Infante, A. P. Pyatakov, S. Fusil, E. Jacquet, C. Carrétéro, C. Deranlot, S. Lisenkov, D. Wang, J. M. Le Breton, M. Cazayous, A. Sacuto, J. Juraszek, A. K. Zvezdin, L. Bellaiche, B. Dkhil, A. Barthélémy, and M. Bibes, "Crafting the magnonic and spintronic response of BiFeO₃ films by epitaxial strain," *Nat Mater*, 12[7] 641-46 (2013).
28. I. C. Infante, S. Lisenkov, B. Dupé, M. Bibes, S. Fusil, E. Jacquet, G. Geneste, S. Petit, A. Courtial, J. Juraszek, L. Bellaiche, A. Barthélémy, and B. Dkhil, "Bridging Multiferroic Phase Transitions by Epitaxial Strain in BiFeO₃," *Physical Review Letters*, 105[5] 057601 (2010).
29. P. Fischer, M. Polomska, I. Sosnowska, and M. Szymanski, "Temperature dependence of the crystal and magnetic structures of BiFeO₃ " *J. Phys. C: Solid State Phys.*, 13[10] 1931 (1980).
30. J. Wang, J. B. Neaton, H. Zheng, V. Nagarajan, S. B. Ogale, B. Liu, D. Viehland, V. Vaithyanathan, D. G. Schlom, U. V. Waghmare, N. A. Spaldin, K. M. Rabe, M. Wuttig, and R. Ramesh, "Epitaxial BiFeO₃ Multiferroic Thin Film Heterostructures," *Science*, 299[5613] 1719-22 (2003).
31. A. Moreira dos Santos, S. Parashar, A. R. Rajub, Y. S. Zhao, A. K. Cheetham, and C. N. R. Rao, "Evidence for the likely occurrence of magnetoelectricity in the simple perovskite, BiMnO₃," *Solid State Communications*, 122[1-2] 49-52 (2002).
32. C. N. R. Rao, A. Sundaresan, and R. Saha, "Multiferroic and Magnetoelectric Oxides: The Emerging Scenario," *J. Phys. Chem. Lett.*, 3[16] 2237-46 (2012).

33. A. Sharan, J. Lettieri, Y. Jia, W. Tian, X. Pan, D. G. Schlom, and V. Gopalan, "Bismuth manganite: A multiferroic with a large nonlinear optical response," *PHYSICAL REVIEW B*, 69[21] 214109 (2004).
34. B. B. Van Aken, T. T. M. Palstra, A. Filippetti, and N. A. Spaldin, "The origin of ferroelectricity in magnetoelectric YMnO₃," *Nat Mater*, 3[3] 164-70 (2004).
35. G. A. Smolenskii and V. A. Bokov, "Coexistence of Magnetic and Electric Ordering in Crystals," *Journal of Applied Physics*, 35[3] 915-18 (1964).
36. Z. J. Huang, Y. Cao, Y. Y. Sun, Y. Y. Xue, and C. W. Chu, "Coupling between the ferroelectric and antiferromagnetic orders in YMnO₃," *PHYSICAL REVIEW B*, 56 2623-26 (1997).
37. N. Ikeda, H. Ohsumi, K. Ohwada, K. Ishii, T. Inami, K. Kakurai, Y. Murakami, K. Yoshii, S. Mori, Y. Horibe, and H. Kito, "Ferroelectricity from iron valence ordering in the charge-frustrated system LuFe₂O₄," *Nature*, 436[7054] 1136-38 (2005).
38. C. R. Serrao, J. R. Sahu, K. Ramesha, and C. N. R. Rao, "Magnetoelectric effect in rare earth ferrites, LnFe₂O₄," *Journal of Applied Physics*, 104[1] - (2008).
39. N. Hur, S. Park, P. A. Sharma, J. S. Ahn, S. Guha, and S. W. Cheong, "Electric polarization reversal and memory in a multiferroic material induced by magnetic fields," *Nature*, 429[6990] 392-95 (2004).
40. T. Goto, T. Kimura, G. Lawes, A. P. Ramirez, and Y. Tokura, "Ferroelectricity and Giant Magnetocapacitance in Perovskite Rare-Earth Manganites," *Phys. Rev. Lett.*, 92[25] 257201 (2004).
41. J. H. Haeni, P. Irvin, W. Chang, R. Uecker, P. Reiche, Y. L. Li, S. Choudhury, W. Tian, M. E. Hawley, B. Craigo, A. K. Tagantsev, X. Q. Pan, S. K. Streiffer, L. Q. Chen, S. W.

- Kirchoefer, J. Levy, and D. G. Schlom, "Room-temperature ferroelectricity in strained SrTiO_3 ," *Nature*, 430[7001] 758-61 (2004).
42. N. Deepak, M. A. Caro, L. Keeney, M. E. Pemble, and R. W. Whatmore, "Interesting Evidence for Template-Induced Ferroelectric Behavior in Ultra-Thin Titanium Dioxide Films Grown on (110) Neodymium Gallium Oxide Substrates," *Advanced Functional Materials* (In press).
 43. K. J. Choi, M. Biegalski, Y. L. Li, A. Sharan, J. Schubert, R. Uecker, P. Reiche, Y. B. Chen, X. Q. Pan, V. Gopalan, L.-Q. Chen, D. G. Schlom, and C. B. Eom, "Enhancement of Ferroelectricity in Strained BaTiO_3 Thin Films," *Science*, 306[5698] 1005-09 (2004).
 44. V. Garcia, M. Bibes, L. Bocher, S. Valencia, F. Kronast, A. Crassous, X. Moya, S. Enouz-Vedrenne, A. Gloter, D. Imhoff, C. Deranlot, N. D. Mathur, S. Fusil, K. Bouzehouane, and A. Barthélémy, "Ferroelectric Control of Spin Polarization," *Science*, 327[5969] 1106-10 (2010).
 45. N. J. C. Ingle and I. S. Elfimov, "Influence of epitaxial strain on the ferromagnetic semiconductor EuO : First-principles calculations," *Phys. Rev. B*, 77 121202-1 to 02-4 (2008).
 46. E. Bousquet, N. A. Spaldin, and P. Ghosez, "Strain-induced Ferroelectricity in Simple Rocksalt Binary Oxides," *Phys. Rev. Lett.*, 104 037601-1 - 01-4 (2010).
 47. C. J. Fennie and K. M. Rabe, "Magnetic and Electric Phase Control in Epitaxial EuTiO_3 from First Principles," *Phys. Rev. Lett.*, 97 267602-1 - 02-4 (2006).
 48. J. H. Lee and K. M. Rabe, "Epitaxial-strain-induced multiferroelectricity in SrMnO_3 from First Principles," *Phys. Rev. Lett.*, 104 207204-1 - 04-4 (2010).

49. V. V. Shvartsman, P. Borisov, K. W., S. Kamba, and T. Katsufuji, "Large off-diagonal magnetoelectric coupling in the quantum paraelectric antiferromagnet EuTiO_3 ," *Phys. Rev. B*, 81 064426-1 to 26-4 (2010).
50. J. H. Lee, L. Fang, E. Vlahos, X. Ke, Y. W. Jung, L. F. Kourkoutis, J.-W. Kim, P. J. Ryan, T. Heeg, M. Roeckerath, V. Goian, M. Bernhagen, R. Uecker, P. C. Hammel, K. M. Rabe, S. Kamba, J. Schubert, J. W. Freeland, D. A. Muller, C. J. Fennie, P. Schiffer, V. Gopalan, E. Johnston-Halperin, and D. G. Schlom, "A strong ferroelectric ferromagnet created by means of spin-lattice coupling," *Nature*, 466[7309] 954-58 (2010).
51. A. Chen, H. Zhou, Z. Bi, Y. Zhu, Z. Luo, A. Bayraktaroglu, J. Phillips, E.-M. Choi, J. L. MacManus-Driscoll, S. J. Pennycook, J. Narayan, Q. Jia, X. Zhang, and H. Wang, "A New Class of Room-Temperature Multiferroic Thin Films with Bismuth-Based Supercell Structure," *Advanced Materials*, 25[7] 1028-32 (2013).
52. B. Aurivillius, "Mixed Bismuth Oxides with Layer Lattice II. Structure of $\text{Bi}_4\text{Ti}_3\text{O}_{12}$," *Ark. Kemi.*, 1 499 (1949).
53. Y. Zhu, A. Chen, H. Zhou, W. Zhang, J. Narayan, J. L. MacManus-Driscoll, Q. Jia, and H. Wang, "Research Updates: Epitaxial strain relaxation and associated interfacial reconstructions: The driving force for creating new structures with integrated functionality," *APL Materials*, 1[5] - (2013).
54. Y. Kitagawa, Y. Hiraoka, T. Honda, T. Ishikura, H. Nakamura, and T. Kimura, "Low-field magnetoelectric effect at room temperature," *Nat. Mater.*, 9[10] 797-802 (2010).
55. L. Wang, D. Wang, Q. Cao, Y. Zheng, H. Xuan, J. Gao, and Y. Du, "Electric control of magnetism at room temperature," *Sci. Rep.*, 2 (2012).

56. D. M. Evans, A. Schilling, A. Kumar, D. Sanchez, N. Ortega, M. Arredondo, R. S. Katiyar, J. M. Gregg, and J. F. Scott, "Magnetic switching of ferroelectric domains at room temperature in multiferroic PZTFT," *Nat. Commun.*, 4 1534 (2013).
57. D. A. Sanchez, N. Ortega, A. Kumar, G. Sreenivasulu, R. S. Katiyar, J. F. Scott, D. M. Evans, M. Arredondo-Arechavala, A. Schilling, and J. M. Gregg, "Room-temperature single phase multiferroic magnetoelectrics: $\text{Pb}(\text{Fe}, \text{M})_x(\text{Zr}, \text{Ti})(1 - x)\text{O}_3$ [$\text{M} = \text{Ta}, \text{Nb}$]," *Journal of Applied Physics*, 113[7] 074105 (2013).
58. J. Schiemer, M. A. Carpenter, D. M. Evans, J. M. Gregg, A. Schilling, M. Arredondo, M. Alexe, D. Sanchez, N. Ortega, R. S. Katiyar, M. Echizen, E. Colliver, S. Dutton, and J. F. Scott, "Studies of the Room-Temperature Multiferroic $\text{Pb}(\text{Fe}_{0.5}\text{Ta}_{0.5})_{0.4}(\text{Zr}_{0.53}\text{Ti}_{0.47})_{0.6}\text{O}_3$: Resonant Ultrasound Spectroscopy, Dielectric, and Magnetic Phenomena," *Advanced Functional Materials*, 10.1002/adfm.201303492 (2014).
59. J. Wang, A. Scholl, H. Zheng, S. B. Ogale, D. Viehland, D. G. Schlom, N. A. Spaldin, K. M. Rabe, M. Wuttig, L. Mohaddes, J. Neaton, U. Waghmare, T. Zhao, and R. Ramesh, "Response to Comment on "Epitaxial BiFeO_3 Multiferroic Thin Film Heterostructures"," *Science*, 307[5713] 1203 (2005).
60. W. Eerenstein, F. D. Morrison, J. Dho, M. G. Blamire, J. F. Scott, and N. D. Mathur, "Comment on "Epitaxial BiFeO_3 Multiferroic Thin Film Heterostructures"," *Science*, 307[5713] 1203 (2005).
61. H. Bea, M. Bibes, S. Fusil, K. Bouzehouane, E. Jacquet, K. Rode, P. Bencok, and A. Barthélémy, "Investigation on the origin of the magnetic moment of BiFeO_3 thin films by advanced x-ray characterisations," *Phys. Rev. B.*, 74 020101 (2006).

62. L. Keeney, S. Kulkarni, N. Deepak, M. Schmidt, N. Petkov, P. F. Zhang, S. Cavill, S. Roy, M. E. Pemble, and R. W. Whatmore, "Room temperature ferroelectric and magnetic investigations and detailed phase analysis of Aurivillius phase $\text{Bi}_5\text{Ti}_3\text{Fe}_{0.7}\text{Co}_{0.3}\text{O}_{15}$ thin films," *Journal of Applied Physics*, 112[5] 052010 (2012).
63. M. Palizdar, T. P. Comyn, M. B. Ward, A. P. Brown, J. P. Harrington, S. Kulkarni, L. Keeney, S. Roy, M. E. Pemble, R. W. Whatmore, C. Quinne, S. H. Kilcoyne, and A. J. Bell, "Crystallographic and Magnetic Identification of Secondary Phase in Oriented $\text{Bi}_5\text{Fe}_{0.5}\text{Co}_{0.5}\text{Ti}_3\text{O}_{15}$ Ceramics," *Journal of Applied Physics*, 112[7] 073919 (2012).
64. S. Patri, R. Choudhary, and B. Samantaray, "Studies of structural, dielectric and impedance properties of $\text{Bi}_9\text{Fe}_5\text{Ti}_3\text{O}_{27}$ ceramics," *J. Electroceram.*, 20[2] 119-26 (2008).
65. P. F. Zhang, N. Deepak, L. Keeney, M. E. Pemble, and R. W. Whatmore, "The structural and piezoresponse properties of c-axis-oriented Aurivillius phase $\text{Bi}_5\text{Ti}_3\text{FeO}_{15}$ thin films deposited by atomic vapor deposition," *Appl. Phys. Lett.*, 101[11] 112903 (2012).
66. S.-I. Ahn, Y. Noguchi, M. Miyayama, and T. Kudo, "Structural and electrical characterization of $\text{Bi}_5\text{Ti}_3\text{Fe}_{1-x}\text{Mn}_x\text{O}_{15}$ system," *Materials Research Bulletin*, 35[6] 825-34 (2000).
67. L. Keeney, C. Groh, S. Kulkarni, S. Roy, M. E. Pemble, and R. W. Whatmore, "Room temperature electromechanical and magnetic investigations of ferroelectric Aurivillius phase $\text{Bi}_5\text{Ti}_3(\text{Fe}_x\text{Mn}_{1-x})\text{O}_{15}$ ($x = 1$ and 0.7) chemical solution deposited thin films," *J. Appl. Phys.*, 112[2] 024101 (2012).
68. N. A. Lomanova, M. I. Morozov, V. L. Ugolkov, and V. V. Gusarov, "Properties of aurivillius phases in the $\text{Bi}_4\text{Ti}_3\text{O}_{12}$ - BiFeO_3 system," *Inorg Mater*, 42[2] 189-95 (2006).
69. D. Y. Suarez, I. M. Reaney, and W. E. Lee, "Relation between tolerance factor and T_c in Aurivillius compounds," *J. Mater. Res.*, 16[11] 3139-49 (2001).

70. A. M. Glazer, "The Classification of Titled Octahedra in Perovskites," *Acta Cryst.*, B28 3384-92 (1972).
71. C. H. Hervoches, A. Snedden, R. Riggs, S. H. Kilcoyne, P. Manuel, and P. Lightfoot, "Structural Behavior of the Four-Layered Aurivillius-Phase Ferroelectrics $\text{SrBi}_4\text{Ti}_4\text{O}_{14}$ and $\text{Bi}_5\text{Ti}_3\text{FeO}_{15}$," *J. Solid State Chem.*, 164 280-91 (2002).
72. N. A. Lomanova, V. G. Semenov, V. V. Panchuk, and V. V. Gusarov, "Structural changes in the homologous series of the Aurivillius phases $\text{Bi}_{n+1}\text{Fe}_n\text{Ti}_3\text{O}_{3n+3}$," *Journal of Alloys and Compounds*, 528[0] 103-08 (2012).
73. A. Sanson and R. W. Whatmore, "Properties of $\text{Bi}_4\text{Ti}_3\text{O}_{12}$ -($\text{Na}_{1/2}\text{Bi}_{1/2}$) TiO_3 Piezoelectric Ceramics," *Jpn. J. Appl. Phys. Part I*, 41[11B] 7127-30 (2002).
74. A. Sanson and R. W. Whatmore, "Phase Diagram of the $\text{Bi}_4\text{Ti}_3\text{O}_{12}$ - BaTiO_3 -($\text{Na}_{1/2}\text{Bi}_{1/2}$) TiO_3 System," *Journal of the American Ceramic Society*, 88[11] 3147-53 (2005).
75. Y. Shimakawa, Y. Kubo, Y. Nakagawa, T. Kamiyama, H. Asano, and F. Izumi, "Crystal structures and ferroelectric properties of $\text{SrBi}_{2-x}\text{Ta}_2\text{O}_9$ and $\text{Sr}_{0.8}\text{Bi}_{2.2}\text{Ta}_2\text{O}_9$," *Applied Physics Letters*, 74[13] 1904-06 (1999).
76. A. Shibuya, M. Noda, and M. Okuyama, "Preparation and Basic Properties of Ferroelectric $\text{Bi}_3\text{TiNbO}_9$ - $\text{Bi}_4\text{Ti}_3\text{O}_{12}$ Thin Films with Different Superlattice Structures," *Ferroelectrics*, 303[1] 83-88 (2004).
77. Y.-I. Kim and M. K. Jeon, "Combined Structural Refinement of $\text{Bi}_4\text{Ti}_3\text{O}_{12}$ using X-ray and neutron powder diffraction data," *Materials Letters*, 58 1889-93 (2004).

78. C. H. Hervoches, A. Snedden, R. Riggs, S. H. Kilcoyne, P. Manuel, and P. Lightfoot, "Structural Behavior of the Four-Layer Aurivillius-Phase Ferroelectrics $\text{SrBi}_4\text{Ti}_4\text{O}_{15}$ and $\text{Bi}_5\text{Ti}_3\text{FeO}_{15}$," *Journal of Solid State Chemistry*, 164[2] 280-91 (2002).
79. "Crystallographica, v1.60d, (c) Oxford Cryosystems Ltd," v1.60d (1995-2007).
80. K. Momma and F. Izumi, "VESTA 3 for three-dimensional visualization of crystal, volumetric and morphology data," *J. Appl. Cryst.*, 44 1272-76 (2011).
81. N. A. Lomanova, M. I. Morozov, V. L. Ugolkov, and V. V. Gusarov, "Properties of aurivillius phases in the $\text{Bi}_4\text{Ti}_3\text{O}_{12}$ - BiFeO_3 system," *Inorg. Mat.*, 42[2] 189-95 (2006).
82. J. S. Anderson, "Non-stoichiometric and Ordered Phases: Thermodynamic Considerations," pp. 1-20. in *The Chemistry of Extended Defects in Non-metallic Solids: Proceedings of the Institute for Advanced Study on the Chemistry of Extended Defects in Non-Metallic Solids*. Edited by L. Eyring and M. O'Keefe. North-Holland Publishing Company - Amsterdam, London, 1969.
83. M. A. Zurbuchen, W. Tian, X. Q. Pan, D. Fong, S. K. Streiffer, M. E. Hawley, J. Lettieri, Y. Jia, G. Asayama, S. J. Fulk, D. J. Comstock, S. Knapp, A. H. Carim, and D. G. Schlom, "Morphology, structure, and nucleation of out-of-phase boundaries (OPBs) in epitaxial films of layered oxides," *Journal of Materials Research*, 22[06] 1439-71 (2007).
84. T. Kobayashi, Y. Noguchi, and M. Miyayama, "Enhanced spontaneous polarization in superlattice-structured $\text{Bi}_4\text{Ti}_3\text{O}_{12}$ - $\text{BaBi}_4\text{Ti}_4\text{O}_{15}$ single crystals," *Applied Physics Letters*, 86[1] - (2005).
85. M. A. Zurbuchen, N. J. Podraza, J. Schubert, Y. Jia, and D. G. Schlom, "Synthesis of the superlattice complex oxide $\text{Sr}_5\text{Bi}_4\text{Ti}_8\text{O}_{27}$ and its band gap behavior," *Applied Physics Letters*, 100[22] - (2012).

86. N. Deepak, P. F. Zhang, L. Keeney, M. E. Pemble, and R. W. Whatmore, "Atomic vapor deposition of bismuth titanate thin films," *Journal of Applied Physics*, 113[18] 187207 (2013).
87. L. Keeney, C. Groh, S. Kulkarni, S. Roy, M. E. Pemble, and R. W. Whatmore, "Room temperature electromechanical and magnetic investigations of ferroelectric Aurivillius phase $\text{Bi}_5\text{Ti}_3(\text{Fe}_x\text{Mn}_{1-x})\text{O}_{15}$ ($x=1$ and 0.7) chemical solution deposited thin films," *Journal of Applied Physics*, 112[2] 024101 (2012).
88. L. Keeney, P. F. Zhang, C. Groh, M. E. Pemble, and R. W. Whatmore, "Piezoresponse force microscopy investigations of Aurivillius phase thin films," *Journal of Applied Physics*, 108[4] 042004 (2010).
89. P. F. Zhang, N. Deepak, L. Keeney, M. E. Pemble, and R. W. Whatmore, "The structural and piezoresponse properties of c-axis-oriented Aurivillius phase $\text{Bi}_5\text{Ti}_3\text{FeO}_{15}$ thin films deposited by atomic vapor deposition," *Applied Physics Letters*, 101[11] 112903 (2012).
90. D. J. Wouters, D. Maes, L. Goux, J. G. Lisoni, V. Paraschiv, J. A. Johnson, M. Schwitters, J.-L. Everaert, W. Boullart, M. Schaekers, M. Willegems, H. Vander Meeren, L. Haspeslagh, C. Artoni, C. Caputa, P. Casella, G. Corallo, G. Russo, R. Zambrano, H. Monchoix, G. Vecchio, and L. Van Autryve, "Integration of $\text{SrBi}_2\text{Ta}_2\text{O}_9$ thin films for high density ferroelectric random access memory," *Journal of Applied Physics*, 100[5] - (2006).
91. B. H. Park, B. S. Kang, S. D. Bu, T. W. Noh, J. Lee, and W. Jo, "Lanthanum-substituted bismuth titanate for use in non-volatile memories," *Nature*, 401[6754] 682-84 (1999).

92. J. Yang, W. Tong, Z. Liu, X. B. Zhu, J. M. Dai, W. H. Song, Z. R. Yang, and Y. P. Sun, "Structural, magnetic, and EPR studies of the Aurivillius phase $\text{Bi}_6\text{Fe}_2\text{Ti}_3\text{O}_{18}$ and $\text{Bi}_6\text{FeCrTi}_3\text{O}_{18}$," *Physical Review B*, 86[10] 104410 (2012).
93. E. Fujii and K. Uchiyama, "First 0.18 μm SBT-Based Embedded FeRAM Technology with Hydrogen Damage Free Stacked Cell Structure," *Integrated Ferroelectrics*, 53[1] 317-23 (2003).
94. C. A. P. de Araujo, J. D. Cuchiaro, L. D. McMillan, M. C. Scott, and J. F. Scott, "Fatigue-free ferroelectric capacitors with platinum electrodes," *Nature*, 374[6523] 627-29 (1995).
95. R. E. Newnham, R. W. Wolfe, and J. F. Dorrian, "Structural Basis of Ferroelectricity in the Bismuth Titanate Family," *Mat. Res. Bull.*, 6 1029-40 (1971).
96. T. Watanabe and H. Funakubo, "Controlled crystal growth of layered-perovskite thin films as an approach to study their basic properties," *Journal of Applied Physics*, 100[5] - (2006).
97. H. Irie, M. Miyayama, and T. Kudo, "Structure dependence of ferroelectric properties of bismuth layer-structured ferroelectric single crystals," *Journal of Applied Physics*, 90[8] 4089-94 (2001).
98. P. Boullay, G. Trolliard, D. Mercurio, J. M. Perez-Mato, and L. Elcoro, "Toward a Unified Approach to the Crystal Chemistry of Aurivillius-Type Compounds.: I. The Structural Model," *Journal of Solid State Chemistry*, 164[2] 252-60 (2002).
99. L. Keeney, C. Groh, S. Kulkarni, S. Roy, M. E. Pemble, and R. W. Whatmore, "Room temperature electromechanical and magnetic investigations of ferroelectric Aurivillius phase $\text{Bi}_5\text{Ti}_3(\text{Fe}_x\text{Mn}_{1-x})\text{O}_{15}$ ($x = 1$ and 0.7) chemical solution deposited thin films," *Journal of Applied Physics*, 112[2] 024101 (2012).

100. X. Y. Mao, W. Wang, and X. B. Chen, "Electrical and magnetic properties of $\text{Bi}_5\text{FeTi}_3\text{O}_{15}$ compound prepared by inserting BiFeO_3 into $\text{Bi}_4\text{Ti}_3\text{O}_{12}$," *Solid State Commun.*, 147[5–6] 186-89 (2008).
101. A. Srinivas, M. M. Kumar, S. V. Suryanarayana, and T. Bhimasankaram, "Investigation of dielectric and magnetic nature of $\text{Bi}_7\text{Fe}_3\text{Ti}_3\text{O}_{21}$," *Materials Research Bulletin*, 34[6] 989-96 (1999).
102. A. Srinivas, D.-W. Kim, K. S. Hong, and S. V. Suryanarayana, "Study of magnetic and magnetoelectric measurements in bismuth iron titanate ceramic— $\text{Bi}_8\text{Fe}_4\text{Ti}_3\text{O}_{24}$," *Materials Research Bulletin*, 39[1] 55-61 (2004).
103. M. A. Zurbuchen, R. S. Freitas, M. J. Wilson, P. Schiffer, M. Roeckerath, J. Schubert, M. D. Biegalski, G. H. Mehta, D. J. Comstock, J. H. Lee, Y. Jia, and D. G. Schlom, "Synthesis and characterization of an $n = 6$ Aurivillius phase incorporating magnetically active manganese, $\text{Bi}_7(\text{Mn,Ti})_6\text{O}_{21}$," *Appl. Phys. Lett.*, 91[3] 033113 (2007).
104. X. Mao, W. Wang, X. Chen, and Y. Lu, "Multiferroic properties of layer-structured $\text{Bi}_5\text{Fe}_{0.5}\text{Co}_{0.5}\text{Ti}_3\text{O}_{15}$ ceramics," *Appl. Phys. Lett.*, 95[8] 082901 (2009).
105. L. Keeney, S. Kulkarni, N. Deepak, M. Schmidt, N. Petkov, P. F. Zhang, S. Cavill, S. Roy, M. E. Pemble, and R. W. Whatmore, "Room temperature ferroelectric and magnetic investigations and detailed phase analysis of Aurivillius phase $\text{Bi}_5\text{Ti}_3\text{Fe}_{0.7}\text{Co}_{0.3}\text{O}_{15}$ thin films," *J. Appl. Phys.*, 112[5] 052010 (2012).
106. M. Palizdar, T. P. Comyn, M. B. Ward, A. P. Brown, J. P. Harrington, S. Kulkarni, L. Keeney, S. Roy, M. E. Pemble, R. W. Whatmore, C. Quinne, S. H. Kilcoyne, and A. J. Bell, "Crystallographic and Magnetic Identification of Secondary Phase in Oriented $\text{Bi}_5\text{Fe}_{0.5}\text{Co}_{0.5}\text{Ti}_3\text{O}_{15}$ Ceramics," *J. Appl. Phys.*, 112[7] 073919 (2012).

107. C.-W. Nan, M. I. Bichurin, S. Dong, D. Viehland, and G. Srinivasan, "Multiferroic magnetoelectric composites: Historical perspective, status, and future directions," *J. Appl. Phys.*, 103[3] 031101 (2008).
108. F. Z. Huang, X. M. Lu, T. T. Xu, Y. Y. Liu, W. N. Su, Y. M. Jin, Y. Kan, and J. S. Zhu, "Multiferroic properties of Co and Nd co-substituted $\text{Bi}_5\text{Ti}_3\text{FeO}_{15}$ thin films," *Thin Solid Films*, 520[21] 6489-92 (2012).
109. J. Yang, W. Tong, Z. Liu, X. B. Zhu, J. M. Dai, W. H. Song, Z. R. Yang, and Y. P. Sun, "Structural, magnetic, and EPR studies of the Aurivillius phase $\text{Bi}_6\text{Fe}_2\text{Ti}_3\text{O}_{18}$ and $\text{Bi}_6\text{FeCrTi}_3\text{O}_{18}$," *Phys. Rev. B*, 86[10] 104410 (2012).
110. J. Yang, L. H. Yin, Z. Liu, X. B. Zhu, W. H. Song, J. M. Dai, Z. R. Yang, and Y. P. Sun, "Magnetic and dielectric properties of Aurivillius phase $\text{Bi}_6\text{Fe}_2\text{Ti}_3\text{O}_{18}$ and the doped compounds," *Appl. Phys. Lett.*, 101[1] 012402 (2012).
111. N. V. Prasad and G. S. Kumar, "Magnetic and magnetoelectric measurements on rare-earth-substituted five-layered $\text{Bi}_6\text{Fe}_2\text{Ti}_3\text{O}_{12}$ compound," *Journal of Magnetism and Magnetic Materials*, 213 349-56 (2000).
112. Z. Liu, J. Yang, X. W. Tang, L. H. Yin, X. B. Zhu, J. M. Dai, and Y. P. Sun, "Multiferroic properties of Aurivillius phase $\text{Bi}_6\text{Fe}_{2-x}\text{Co}_x\text{Ti}_3\text{O}_{18}$ thin films prepared by a chemical solution deposition route," *Appl. Phys. Lett.*, 101[12] (2012).
113. M. Schumacher, P. K. Baumann, and T. Seidel, "AVD and ALD as Two Complementary Technology Solutions for Next Generation Dielectric and Conductive Thin-Film Processing," *Chemical Vapor Deposition*, 12[2-3] 99-108 (2006).

114. D. A. Hope, A. K. Cheetham, and G. J. Long, "A Neutron Diffraction, Magnetic Susceptibility, and Mossbauer-Effect Study of the (Mn,Fel-)yO Solid Solutions," *Inorganic Chemistry*, 21 2804-09 (1982).
115. J.-B. Li, Y. P. Huang, G. H. Rao, G. Y. Liu, J. Luo, J. R. Chen, and J. K. Liang, "Ferroelectric transition of Aurivillius compounds Bi₅Ti₃FeO₁₅ and Bi₆Ti₃Fe₂O₁₈," *Applied Physics Letters*, 96[22] - (2010).
116. Z. Liu, J. Yang, X. W. Tang, L. H. Yin, X. B. Zhu, J. M. Dai, and Y. P. Sun, "Multiferroic properties of Aurivillius phase Bi₆Fe_{2-x}CoxTi₃O₁₈ thin films prepared by a chemical solution deposition route," *Applied Physics Letters*, 101[12] - (2012).
117. S. V. Kalinin, A. Gruverman, and D. A. Bonnell, "Quantitative analysis of nanoscale switching in SrBi₂Ta₂O₉ thin films by piezoresponse force microscopy," *Appl. Phys. Lett.*, 85[5] 795-97 (2004).
118. S. V. Kalinin, B. J. Rodriguez, S. Jesse, E. Karapetian, B. Mirman, E. A. Eliseev, and A. N. Morozovska, "Nanoscale Electromechanics of Ferroelectric and Biological Systems: A New Dimension in Scanning Probe Microscopy," *Ann. Rev. of Mater. Res.*, 37[1] 189-238 (2007).
119. J. Varghese, S. Barth, L. Keeney, R. W. Whatmore, and J. D. Holmes, "Nanoscale Ferroelectric and Piezoelectric Properties of Sb₂S₃ Nanowire Arrays," *Nano Lett.*, 12[2] 868-72 (2012).
120. S. V. Kalinin, Z.-G. Ye, and A. L. Kholkin, "Preface to Special Topic: Piezoresponse Force Microscopy and Nanoscale Phenomena in Polar Materials," *J. Appl. Phys.*, 112[5] 051901 (2012).

121. S. V. Kalinin, N. Setter, and A. L. Kholkin, "Electromechanics on the Nanometer Scale: Emerging Phenomena, Devices, and Applications," *Mrs Bulletin*, 34[09] 634-42 (2009).
122. B. J. Rodriguez, C. Callahan, S. V. Kalinin, and R. Proksch, "Dual-frequency resonance-tracking atomic force microscopy," *Nanotechnology*, 18[47] 475504 (2007).
123. X. Y. Mao, W. Wang, and X. B. Chen, "Electrical and magnetic properties of Bi₅FeTi₃O₁₅ compound prepared by inserting BiFeO₃ into Bi₄Ti₃O₁₂," *Solid State Communications*, 147[5-6] 186-89 (2008).
124. A. Srinivas, D.-W. Kim, K. S. Hong, and S. V. Suryanarayana, "Observation of ferroelectromagnetic nature in rare-earth-substituted bismuth iron titanate," *Applied Physics Letters*, 83[11] 2217-19 (2003).
125. J. Zhu, X.-y. Mao, and X.-b. Chen, "Properties of vanadium-doped SrBi₄Ti₄O₁₅ ferroelectric ceramics," *Solid State Communications*, 129[11] 707-10 (2004).
126. M. A. Zurbuchen, R. S. Freitas, M. J. Wilson, P. Schiffer, M. Roeckerath, J. Schubert, M. D. Biegalski, G. H. Mehta, D. J. Comstock, J. H. Lee, Y. Jia, and D. G. Schlom, "Synthesis and characterization of an n = 6 Aurivillius phase incorporating magnetically active manganese, Bi₇(Mn,Ti)₆O₂₁," *Applied Physics Letters*, 91[3] 033113 (2007).
127. X. Mao, W. Wang, X. Chen, and Y. Lu, "Multiferroic properties of layer-structured Bi₅Fe_{0.5}Co_{0.5}Ti₃O₁₅ ceramics," *Applied Physics Letters*, 95[8] 082901 (2009).
128. J. Yang, L. H. Yin, Z. Liu, X. B. Zhu, W. H. Song, J. M. Dai, Z. R. Yang, and Y. P. Sun, "Magnetic and dielectric properties of Aurivillius phase Bi₆Fe₂Ti₃O₁₈ and the doped compounds," *Applied Physics Letters*, 101[1] 012402 (2012).
129. J. Lu, L. J. Qiao, X. Q. Ma, and W. Y. Chu, "Magnetodielectric effect of Bi₆Fe₂Ti₃O₁₈ film under an ultra-low magnetic field," *J. Phys.: Condens. Mater.*, 18 4801-07 (2006).

130. A. Srinivas, S. V. Suryanarayana, G. S. Kumar, and M. M. Kumar, "Magnetoelectric measurements on Bi₅FeTi₃O₁₅ and Bi₆Fe₂Ti₃O₁₈," *J. Phys.: Condens. Mater.*, 11 3335-40 (1999).
131. N. Guan, Y. Wang, D. Sun, and J. Xu, "A simple one-pot synthesis of single-crystalline magnetite hollow spheres from a single iron precursor," *Nanotechnology*, 20[10] 105603 (2009).
132. G. Goya, T. Berquo, F. Fonseca, and M. Morales, "Static and dynamic magnetic properties of spherical magnetite nanoparticles," *Journal of Applied Physics*, 94[5] 3520-28 (2003).
133. G. E. Moore, "Cramming More Components onto Integrated Circuits," *Electronics* 114-17 (1965).
134. E. Y. Tsymbal and A. Gruverman, "Ferroelectric tunnel junctions: Beyond the barrier," *Nat Mater*, 12[7] 602-04 (2013).
135. V. Garcia and M. Bibes, "Electronics: Inside story of ferroelectric memories," *Nature*, 483[7389] 279-81 (2012).
136. L. Esaki, "Long Journey into Tunneling," *Science*, 183[4130] 1149-55 (1974).
137. J. F. Scott, "Applications of magnetoelectrics," *Journal of Materials Chemistry*, 22[11] 4567-74 (2012).
138. A. Roy, R. Gupta, and A. Garg, "Multiferroic Memories," *Advances in Condensed Matter Physics*, 2012 12 (2012).
139. M. Bibes and A. Barthelémy, "Multiferroics: Towards a magnetoelectric memory," *Nat Mater*, 7[6] 425-26 (2008).
140. Y.-H. Chu, L. W. Martin, M. B. Holcomb, M. Gajek, S.-J. Han, Q. He, N. Balke, C.-H. Yang, D. Lee, W. Hu, Q. Zhan, P.-L. Yang, A. Fraile-Rodriguez, A. Scholl, S. X. Wang,

- and R. Ramesh, "Electric-field control of local ferromagnetism using a magnetoelectric multiferroic," *Nat Mater*, 7[6] 478-82 (2008).
141. M. Fiebig, T. Lottermoser, M. K. Kneip, and M. Bayer, "Correlations between magnetic and electrical orderings in multiferroic manganites (invited)," *Journal of Applied Physics*, 99[8] 08E302 (2006).
142. J. F. Scott, "Data storage: Multiferroic memories," *Nat Mater*, 6[4] 256-57 (2007).
143. D. D. Fong, G. B. Stephenson, S. K. Streiffer, J. A. Eastman, O. Auciello, P. H. Fuoss, and C. Thompson, "Ferroelectricity in Ultrathin Perovskite Films," *Science*, 304[5677] 1650-53 (2004).
144. M. Bibes, "Nanoferronics is a winning combination," *Nat Mater*, 11[5] 354-57 (2012).
145. M. Bibes, J. E. Villegas, and A. Barthélémy, "Ultrathin oxide films and interfaces for electronics and spintronics," *Advances in Physics*, 60[1] 5-84 (2011).

List of Figures and Tables:

Fig. 1.1. The relationship between multiferroic and magnetoelectric materials. (Redrawn from^{1, 2}).

Fig. 1.2. Scanning transmission electron microscopy (STEM) images of **(a)** $\text{Bi}_2\text{FeMnO}_6$ structure obtained on $\text{SrTiO}_3(001)$ and **(b)** the new $\text{Bi}_3\text{Fe}_2\text{Mn}_2\text{O}_x$ (BFMO322) supercell structure obtained on LaAlO_3 substrates. **(c)** Displays the increased magnification image of the region outlined in (b) demonstrating the coherent interface between the LaAlO_3 substrate and the BFMO interlayer. From Chen *et al.*⁵¹

Fig. 1.3. Ferroelectric domain configurations of $[\text{Pb}(\text{Zr}_{0.53}\text{Ti}_{0.47})\text{O}_3]_{0.6}-[\text{Pb}(\text{Fe}_{0.5}\text{Ta}_{0.5})\text{O}_3]_{0.4}$ changing dramatically with an applied magnetic field.⁵⁶ Lateral piezoresponse force microscopy images before **(a)** and after **(b)** the application of 1.8 T magnetic field.

Figure 2.1. a -axis (plus 4°) projection of the $m = 4$ Aurivillius phase $\text{Bi}_5\text{Ti}_3\text{FeO}_{15}$. Drawn using structural parameters from Hervoches *et al.*,⁷⁸ Crystallographica v1.60d⁷⁹ and VESTA 3.0 3D visualization program for crystal structures⁸⁰.

Fig. 2.2. Images of BTF7M3O on $\text{SiO}_2\text{-Si}$: (a) topography, (b) out-of-plane PFM (piezoresponse force microscopy) amplitude, and (c) out-of-plane PFM phase after PFM lithography with an applied dc bias of 33.0 V.⁹⁹

Fig. 2.3. (a) XAS-PEEM image at Fe L-edge resonance (707.32 eV) and (b) XMCD-PEEM image at Fe L-edge resonance (707.32 eV) demonstrating magnetic signature at the Fe edge for the Fe-rich inclusions. (c) XAS-PEEM image at Co L-edge resonance (775.75 eV) and (d) XMCD-PEEM image at Co L-edge resonance (775.75 eV) demonstrating no magnetic signature at the Co edge for the Co-rich inclusions. Frame of view is $6\text{ }\mu\text{m}$.⁶²

Fig. 3.1.1. (a) TEM image taken from a cross section of the annealed $\text{Bi}_5\text{Ti}_3\text{FeO}_{15}$ film. (b) HRTEM image of the lattice structure.¹¹²

Fig. 3.1.2. (a) XRD patterns from B7TFO and B6TFMO thin films, (b) HR-TEM image and (c) electron diffraction pattern of B6TFMO.²

Fig. 3.2.1. Vertical DART-PFM switching spectroscopy (a) phase and (b) piezoresponse loops of B7TFO and (c) phase and (d) piezoresponse loops of B6TFMO thin films in the absence of an applied DC bias. Images of B6TFMO on c-plane sapphire: (e) out-of-plane PFM phase and (f) out-of-plane PFM amplitude after PFM lithography with an applied electric field of 70 V.²

Fig. 3.3.1. Typical Zero Field Cooled (ZFC) – Field Cooled (FC) – Remanence curve (a) and magnetic hysteresis (MH) loop (b) measured in SQUID magnetometer.²

Fig. 3.3.2. The magnetic properties of B7TFO phase were investigated. Figure (a) shows the magnetic hysteresis measured at 2K and the inset shows hysteresis after direct subtraction of the diamagnetic substrate contribution. Figure (b) shows the zoomed hysteresis loop of B6TFMO measured at different temperatures.

Fig. 3.3.3 (a) Electronic Arrangement of 5 *d* electrons in “low spin” and “high-spin” configurations and (b) mechanism for ferromagnetic ordering.

Fig. 3.4.1 Representative images of B6TFMO thin films: (a) topography; (c) lateral PFM amplitude; and (e) lateral PFM phase under 0 mT H field and (b) topography; (d) lateral PFM; and (f) lateral PFM phase under +250 mT H field.²

Fig. 3.4.2. Representative images of B6TFMO thin films: (a) topography; (b) vertical PFM amplitude; and (c) vertical PFM phase under 0 mT H field; (d) topography; (e) vertical PFM

amplitude; and (f) vertical PFM phase under +250 mT H field; and (g) topography; (h) vertical PFM amplitude; and (i) vertical PFM phase under -250 mT H field.²

Fig. 4.1. Remanent magnetization $M_{r,F}$ of Fe_3O_4 as function of grain size. The blue line shows literature data from ¹³¹ (blue dots) and ¹³² (red dot). Because there are only a few literature values, a conveniently chosen (piecewise constant) green line is chosen which is assumed to conservatively overestimate (up to the chosen confidence level) the true remanent magnetization for all grain sizes d .

Fig. 5.1. Dynamic switching device structure. Three dimensional (a) and cross-sectional (b) schematic diagram of the co-planar epitaxial electrode device showing a structure that could enable controlled ferroelectric switching and electrical control of ferromagnetism.¹⁴⁰

Fig. 5.2. The binary information is stored by the magnetization direction of the bottom ferromagnetic layer (blue), read by the resistance of the magnetic trilayer (R_p when the magnetizations of the two ferromagnetic layers are parallel), and written by applying a voltage across the multiferroic ferroelectric antiferromagnetic layer (FE-AFM; green). If the magnetization of the bottom ferromagnetic layer is coupled to the spins in the multiferroic (small white arrows) and if the magnetoelectric coupling is strong enough, reversing the ferroelectric polarization P in the multiferroic changes the magnetic configuration in the trilayer from parallel to antiparallel, and the resistance from R_p to antiparallel (R_{ap}). A hysteretic dependence of the device resistance with voltage is achieved (blue curve).¹³⁹

Fig. 5.3. Image of a possible single-phase multiferroic magnetic field sensor where the multiferroic material is sandwiched in between two magnetic electrode layers.

List of Figures Requiring Copyright Permission:

Fig. 1.2. Permission Granted from John Wiley and Sons. Licence number: 3363560925963.

Fig. 1.3. Permission Granted from Nature Publishing Group. Licence number: 3363570082676.

Fig. 2.2. Permission Granted from AIP Publishing LLC. Licence number: 3363570616689.

Fig. 2.3. Permission Granted from AIP Publishing LLC. Licence number: 3363570895076.

Fig. 3.1.1. Permission Granted from AIP Publishing LLC. Licence number: 3363590609117.

Fig. 3.1.2. Permission Granted from John Wiley and Sons. Licence number: 3363560395267.

Fig. 3.2.1. Permission Granted from John Wiley and Sons. Licence number: 3363560395267.

Fig. 3.3.1. Permission Granted from John Wiley and Sons. Licence number: 3363560395267.

Fig. 3.4.1. Permission Granted from John Wiley and Sons. Licence number: 3363560395267.

Fig. 3.4.2. Permission Granted from John Wiley and Sons. Licence number: 3363560395267.

Fig. 5.1. Permission Granted from Nature Publishing Group. Licence number: 3364890398035.

Fig. 5.2. Permission Granted from Nature Publishing Group. Licence number: 336300849035.